

**COUPLING AND SYNCHRONY IN NEURONAL NETWORKS:
ELECTROPHYSIOLOGICAL STUDIES**

A Dissertation
Presented to
The Academic Faculty

by

Amanda Jervis Preyer

In Partial Fulfillment
Of the Requirements for the Degree
Doctor of Philosophy in the
School of Electrical and Computer Engineering

Georgia Institute of Technology
August 2007

Copyright © Amanda Jervis Preyer 2007

**COUPLING AND SYNCHRONY IN NEURONAL NETWORKS:
ELECTROPHYSIOLOGICAL STUDIES**

Approved by:

Dr. Robert Butera, Advisor
School of Electrical and Computer
Engineering
Georgia Institute of Technology

Dr. Carmen Canavier
School of Medicine
Louisiana State University

Dr. Stephen DeWeerth
School of Electrical and Computer
Engineering
Georgia Institute of Technology

Dr. Paul Hasler
School of Electrical and Computer
Engineering
Georgia Institute of Technology

Dr. Aaron Lanterman
School of Electrical and Computer
Engineering
Georgia Institute of Technology

Dr. Astrid Prinz
Department of Biological and
Biomedical Sciences
Emory University

Date Approved: July 2, 2007 □

ACKNOWLEDGEMENTS

I would like to take this opportunity to thank several of the people who helped me throughout my graduate experience. First, I would like to thank my advisor, Rob Butera, who made significant intellectual contributions to this work. He provided guidance when I needed it and let me go when I didn't. He also understood that there is more to life than research. I would not have made it this far without his guidance.

I would like to thank the members of my PhD committee for the time they have invested in this project. I would especially like to thank Carmen Canavier who provided important insight into the research and was willing to travel from New Orleans to help. I would also like to thank Astrid Prinz for her contributions.

I would like to thank the past and present members of the Butera group for making my graduate experience a lot more fun, especially my officemates Luke Purvis, Murat Sekerli, and Laveeta Joseph who provided many opportunities for procrastination. I would also like to thank Carrie Williams.

I would like to thank my family and friends for all of their love and support. My family is by far my greatest asset. Thank you Mom, Dad, and Katie, for everything and especially Melissa for being my biggest cheerleader.

Finally, I'd like to thank my boys, Justin and Andrew, for everything you are and do for me.

TABLE OF CONTENTS

ACKNOWLEDGEMENTS.....	III
LIST OF TABLES.....	VII
LIST OF FIGURES.....	VIII
SUMMARY.....	X
CHAPTER 1: INTRODUCTION AND BACKGROUND.....	1
1.1 Introduction.....	1
1.2 Specific Aims.....	4
1.3 Background and Significance.....	5
1.3.1 Electrophysiology Experiments.....	5
1.3.2 Dynamic Clamp Technique.....	7
1.3.3 Phase Response Curves.....	11
1.3.4 Weak Coupling.....	14
1.3.5 Coupling and Synchrony in Inhibitory Networks.....	15
CHAPTER 2: WEAK COUPLING.....	19
2.1 Methods.....	19
2.1.1 Linear Scaling.....	20
2.1.2 IPRCs.....	21
2.2 Results.....	24
2.2.1 Linear Scaling.....	24
2.2.2 IPRCs.....	25
2.3 Discussion.....	26
CHAPTER 3: COUPLING AND PHASE RESPONSE CURVES.....	29

3.1 Methods.....	31
3.1.1 Computational Models.....	31
3.1.2 Coupling Experiments.....	33
3.1.3 PRC Existence and Stability Criteria.....	35
3.1.4 PRC Emulator.....	37
3.1.5 Data Analysis.....	39
3.2 Results.....	43
3.2.1 Predicted and Observed Modes of Synchrony.....	43
3.2.2 Transitions from Anti-Phase to In-Phase Synchrony.....	45
3.2.3 Synchrony Predicted by PRCs.....	47
3.3 Discussion.....	49
CHAPTER 4: DYNAMIC CLAMP STABILITY.....	52
4.1 Methods.....	53
4.1.1 Physical Experiments.....	53
4.1.2 Computational Model System.....	54
4.1.3 Simulations and Stability Analysis.....	61
4.2 Results.....	62
4.2.1 Physical Experiment and Simple Electrode Model Results.....	62
4.2.2 Electrode and Amplifier Model.....	69
4.3 Discussion.....	74
CHAPTER 5: CONCLUSIONS.....	79
5.1 Weak Coupling.....	810
5.2 Coupling and Phase Response Curves.....	81

5.3 Dynamic Clamp Stability.....	82
5.4 Conclusions.....	84
APPENDIX A: WANG AND BUZSAKI MODEL NEURON.....	85
REFERENCES.....	87
VITA.....	94

LIST OF TABLES

Table 1: MSE results.....	24
Table 2: Parameter values for full electrode and amplifier model.....	60
Table 3: Parameters used with the Wang and Buzsaki computational model.	86

LIST OF FIGURES

Figure 1: Block diagram of electrophysiology setup with dynamic clamp	7
Figure 2: The effect of a perturbation on spike timing..	12
Figure 3: Phase Response Curve.....	13
Figure 4: Phase difference between two identical oscillators	17
Figure 5: Linear scaling of PRCs.....	21
Figure 6: Matched conductances and PRCs.....	22
Figure 7: IPRCs and reconstructed PRCs	23
Figure 8: MSE as a function of PRC amplitude.....	26
Figure 9: Matched PRCs from a live neuron and a Wang and Buzsaki model.....	33
Figure 10: PRCs and smoothing spline curve fits.....	38
Figure 11: Example traces from the phase model simulator.....	39
Figure 12: Example of how phase difference is calculated for coupled neurons.....	40
Figure 13: Phase difference raster plots and histograms.....	41
Figure 14: Example histogram and pseudocolor plots for multiple τ 's.	43
Figure 15: Qualitative bistability results	44
Figure 16: Pseudocolor plots of histograms from experimental coupling	46
Figure 17: Pseudocolor plots of histograms for experimental, simulation, and analytical data	48
Figure 18: Computational neuron models.....	55
Figure 19: Electrode model with passive membrane	56
Figure 20: Electrode and amplifier model	58
Figure 21: Instability demonstrated in a live neuron	64

Figure 22: Experiments and simulations demonstrating dynamic clamp instability.	65
Figure 23: Maximum stable step conductance as a function of sampling rate and electrode resistance	67
Figure 24: Effect of capacitance on maximum stable conductance	68
Figure 25: Sampling and holding and maximum stable conductance step size.....	69
Figure 26: Maximum stable conductance as a function of P_{cc} and P_{bb}	71
Figure 27: The effect of sampling rate on the maximum stable conductance.	73
Figure 28: The effect of C_{cur} on the maximal stable conductance	74

SUMMARY

There is a significant amount of computational literature on networks of neurons and their resulting behavior. This dissertation combines electrophysiology experiments with computational modeling to validate the assumptions and results found in this literature. First, we investigate the weak coupling assumption, which states that the phase response of a neuron to weak stimuli is separable from the stimulus waveform. For weak stimuli, there is an intrinsic neuronal property described by the infinitesimal phase response curve (IPRC) that will predict the phase response when convolved with the stimulus waveform. Here, we show that there is a linear relationship between the stimulus and phase response of the neuron, and that we are able to obtain IPRCs that successfully predict the neuronal phase response. Next, we use hybrid networks of neurons to study the phase locking behavior of networks as the synaptic time constant is changed. We verify that networks show anti-phase synchrony for fast time constants, and in-phase synchrony for slow time constants. We also show that phase models and phase response curves (PRCs) qualitatively predict phase locking observed in electrophysiology experiments. Finally, we investigate the stability of the dynamic clamp system. We determined that the maximal conductance of the current being simulated, the dynamic clamp sampling rate, the amount of electrode resistance compensation, and the amount of capacitance compensation all affect when the instability is present. There is a dramatic increase in stability when the electrode resistance and system capacitance are well compensated.

CHAPTER 1

INTRODUCTION AND BACKGROUND

The information processing power of the human nervous system far exceeds our current technological state of the art. With millions of neurons we are able to perform a wide variety of tasks, including receiving, combining, and interpreting information from various sensory modalities. This information is used to make decisions, store memories, and determine and execute motor output. While we have some rudimentary ideas of how these tasks are performed, we are far from a thorough understanding of how networks of individual neurons work. As our knowledge of neurological systems grows, we will be able to repair or replace nervous system functionality lost through illness and accident, and produce better technology by incorporating techniques used by the nervous system.

1.1 Introduction

The nervous system is a complex information processing structure made up of networks of thousands of neurons coupled together. It integrates information efficiently and robustly through a highly parallelized structure. Information transfer and processing take place through a variety of mechanisms. One important example of this is temporal coding (Cariani 2004). Layers of neurons integrate information using both the properties of the individual neurons and the synaptic connections between them. The resulting information is stored in the phase relationships between firing neurons. Phase locking and synchrony are common examples of temporal coding.

Synchrony is frequently observed in the nervous system. It has been noted in various places in the cortex. (Schnitzler and Gross 2005; Steriade 1997). In the γ band, it

has been proposed as a mechanism that may perform binding of sensory and cognitive information (Engel et al. 2001; Gray 1999; Singer 1999; Ward 2003). It also plays an important role in motor control and sensory feedback, especially in the 6-9 Hz range. In this range, coherence between EMG recordings and MEG recordings of contralateral sensorimotor cortex show significant correlation (Gross et al. 2002). Abnormal synchronization has been demonstrated in cognitive and movement disorders, such as Parkinson's disease, epilepsy, and schizophrenia (Hutchinson et al. 2004; Stelt et al. 2004; Timofeev and Steriade 2004). Mental tasks that require heavy usage of working memory increase both within-frequency synchrony and cross-frequency synchronization of α , β , and γ oscillations (Palva et al. 2005). Finally, synchrony is also found in other organ systems of electrically excitable cells. For example, heart pacemaker cells are used to create and maintain the heartbeat, while pancreatic β -cells that secrete insulin also fire synchronously (Jalife 1984; Sherman et al. 1988). Examples of synchrony are also found throughout biology (Mirollo and Strogatz 1990; Pavlidis 1973; Winfree 2001).

Though phase locking and synchrony are prevalent in the nervous system, it is difficult to study how networks produce this activity. *In vivo*, it is impossible to examine and manipulate more than a few neurons at a time, making it difficult to study phase relationships among neurons. Extracellular techniques can be used; however, as the number of neurons being recorded from increases, the amount of information known about each neuron drastically decreases. It is also impossible to measure and manipulate the synapse parameters and connectivity patterns that make up large biological networks *in vivo* and *in vitro*. Computational studies have aided our understanding of the behavior produced by large networks of neurons; however, the models used in simulations must be

simplified to simulate large numbers of neurons. This makes it difficult to replicate the richness and variety found in biology. Often, the results of computational simulations heavily depend on the assumptions used.

Computational modeling and biological experiments are complementary techniques. Computational simulations help us to understand the mechanisms in biology that create synchrony. They predict how biological networks will behave and provide information about the types of properties that should be examined experimentally (Chow 1998; Ermentrout and Kopell 1990b; Hansel et al. 1993; 1995; Sherman and Rinzel 1992; Van Vreeswijk et al. 1994). On the other hand, biological experiments are important for verifying assumptions made in computational simulations and validating their results. This is often done with simple biological systems, including hybrid networks (Galan et al. 2005; Merriam et al. 2005; Netoff et al. 2005b; Pervouchine et al. 2006). These hybrid preparations are used to develop basic principles, which can be adapted to more complex systems, such as the human nervous system.

Currently, there is a large amount of computational theory examining how networks of neurons behave when they are coupled together (Chow 1998; Ermentrout and Kopell 1990a; Hansel et al. 1993; 1995; Sherman and Rinzel 1992; Van Vreeswijk et al. 1994); however, there is significantly less experimental work validating these theoretical predictions (Merriam et al. 2005; Netoff et al. 2005a; Netoff et al. 2005b; Pervouchine et al. 2006; Preyer and Butera 2005). This is mostly due to the difficulty of doing these experiments. Biological systems are significantly noisier, more heterogeneous and less predictable than the computational work. The focus of this research is to use biological experiments to examine some of the theoretical assumptions

and predictions from computational modeling of neuronal networks. In addition, we will examine a commonly used tool for doing these types of experiments, the dynamic clamp.

1.2 Specific Aims

The long term goal of this work is to use the dynamic clamp technique to bridge the gap between theoretical research and electrophysiology experiments with respect to coupling and synchrony in neurons. In particular, we will use the dynamic clamp technique to validate a common assumption used in most phase model analyses of coupling and synchrony, known as the weak coupling assumption. We will also examine how well phase model predictions of synchrony and phase locking in pairs of coupled neurons reflect the behavior of hybrid networks of neurons. Finally, we will examine the stability of the dynamic clamp technique used to perform these experiments.

1. Validate the existence of weak coupling in living neurons. The weak coupling assumption is commonly used in computational studies of networks of coupled neurons, but has never been demonstrated in living cells. We will do this by first testing the linearity of neuronal phase response curves (PRCs) generated in response to weak stimuli. We will then derive infinitesimal phase response curves (IPRCs) from experimentally obtained PRCs and use them to predict the phase response of live neurons to stimuli of different shapes. The results will be quantified by measuring the mean squared error (MSE) between the predicted phase response and the actual phase response.

2. Examine how well predictions of phase-locking made with experimentally measured PRCs match the network behavior of pairs of neurons coupled with inhibitory synapses. Computational literature based on phase models predicts a change from anti-phase to in-phase synchrony for pulse coupled and weakly coupled oscillators

as the coupling time constant is increased. In this aim, we will measure PRCs from live neurons and Wang and Buzsaki computational models and use them to create phase models of hybrid networks of two neurons. We will investigate how simulations of phase models, based on experimentally measured PRCs, predict the phase locked solutions found in electrophysiology coupling experiments. We will also use the PRCs to analytically predict phase locking. This research will focus on transitions from anti-phase to in-phase synchrony that occur when the rate of synaptic coupling is increased, and examine the predicted transition from anti-phase to in-phase synchrony.

3. Investigate stability of the dynamic clamp system. In this aim, we will examine the dynamic clamp technique that was used to perform Aims 1 and 2. During dynamic clamp experiments the system can become unstable, characterized by either a transient oscillation or total instability. We will explore the conditions that cause dynamic clamp instability, focusing on the dynamic clamp sampling rate, the uncompensated series electrode resistance, and the electrode and amplifier capacitance. After exploring the phenomena with the physical experimental setup, we will construct a computational model of delay differential equations. This model will be used to investigate how these factors affect the observed instability in simulation.

1.3 Background and Significance

1.3.1 Electrophysiology Experiments

A significant portion of this project included biological experiments on neurons from the mollusk *Aplysia californica*. Invertebrate animals have significantly simpler nervous systems than vertebrates. In spite of having fewer neurons that are larger and more robust than vertebrate animals, invertebrates use many of the same basic

mechanisms present in vertebrate neurons. As a result, they provide an effective model for studying neuronal mechanisms, with results that can be related to more complex vertebrate systems.

The experiments in this project depend heavily on coupling and phase response theory. As a result, tonically firing cells with extremely low variability and no extraneous input are essential. There are several cells in the abdominal ganglia of *Aplysia* that match these criteria, including L7, L8, and L9 (Frazier et al. 1967). These are regularly spiking neurons previously studied by Perkel (Kandel 1976; Perkel et al. 1964), which spike with periods of 200 – 500 ms. The firing rate is typically quite regular, with the coefficient of variation of the interspike interval varying from .0072 to .1549, with a mean of .0436 (Preyer and Butera 2005). We were able to block synaptic input with a high magnesium, low calcium solution, providing a preparation that met all of our requirements.

Methods

The abdominal ganglia of *Aplysia californica* was removed from the animal, pinned to a Sylgard lined dish, and surgically desheathed in a high magnesium desheathing solution. Intracellular recording was performed with sharp microelectrodes (6 – 12 M Ω) filled with 3 M potassium acetate. Neurons were identified visually and by their electrophysiological properties. Unless otherwise noted, recording was done with bridge balance compensation using an Axoclamp-2B electrophysiology amplifier (Molecular Devices Corporation, Sunnyvale, CA). Signals were then filtered with a Brownlee Precision Model 440 (Brownlee Precision Co., San Jose, CA), and acquired using a Digidata 1322A (Molecular Devices Corporation, Sunnyvale, CA). ClampEx 8.0 (Molecular Devices Corporation, Sunnyvale, CA) software was used to control the

electrophysiology amplifier, and record the current and voltage measurements from the cells. A block diagram is shown in Figure 1.

System Block Diagram

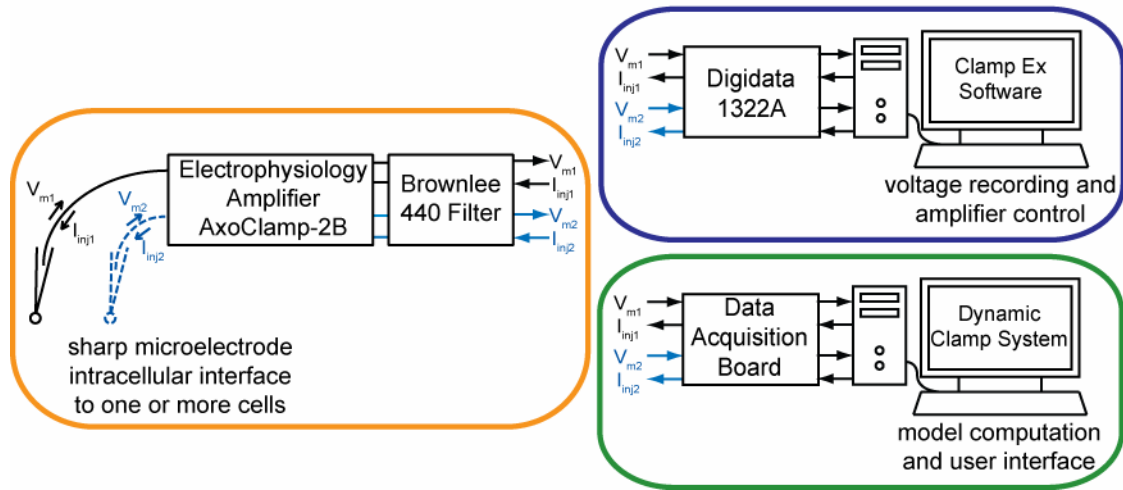


Figure 1. Block diagram of electrophysiology setup with dynamic clamp. The orange section represents standard electrophysiological techniques, including sharp microelectrode recording using the AxoClamp-2B amplifier with external filtering. The blue square represents the ClampEx software system, while the green depicts the dynamic clamp system and its connections.

To suppress synaptic input, recording was done using a high magnesium, low calcium solution, (in mM): NaCl, 330; KCl, 10; MgCl₂, 90; MgSO₄, 20; CaCl₂, 2; HEPES, 10 (Nowotny et al. 2003).

1.3.2 Dynamic Clamp Technique

The dynamic clamp technique is commonly used to combine computational models with electrophysiological experiments. It is an extremely versatile tool that enables an electrophysiologist to artificially create voltage-dependent and time-dependent conductances within neurons (Robinson and Kawai 1993; Sharp et al. 1993a; b) and other excitable cells (Kinard et al. 1999; Wilders 2006). This ability has significantly contributed to our knowledge of neuronal function through the wide variety of experiments it makes possible (Goaillard and Marder 2006; Prinz et al. 2004). Using real-

time feedback, the dynamic clamp makes it possible to add new types of ion channels to a cell, or enhance and depress the contribution of existing channels (Gramoll et al. 1994; Ma and Koester 1996; Ulrich and Huguenard 1996; Zhang et al. 2003). The dynamic clamp is also frequently used to study networks of neurons by creating synaptic conductances that depend on the membrane voltage of a presynaptic cell (Sharp et al. 1996). These networks can either be exclusively biological neurons (Sharp et al. 1996; Verheijck et al. 1998) or hybrid networks, which combine live neurons and computational ones simulated by the dynamic clamp system (Kumar et al. 1996; Manor and Nadim 2001; Merriam et al. 2005; Netoff et al. 2005b; Oprisan et al. 2004).

This project contains experiments that use the dynamic clamp to create computational synaptic currents within cells. Aim 1, investigating weak coupling, uses the dynamic clamp to generate PRCs by injecting a stimulus current with an alpha-shaped conductance waveform. Aim 2 of this project uses the dynamic clamp to synaptically couple two neurons, by coupling a live neuron to a computational model neuron. In this configuration, the dynamic clamp is used to simulate both the model neuron and the artificial synaptic coupling between neurons. Finally, Aim 3 investigates how properties of the dynamic clamp system affect its stability.

Methods

There are several implementations of the dynamic clamp system that are commonly used (Butera et al. 2001; Dorval et al. 2001; Le Masson 1995; Lien and Jonas 2003; Pinto et al. 2001; Preyer 2002). The experiments in this project were performed with the Real-Time Linux based Model Reference Current Injection System (MRCI) (Raikov et al. 2004). With this setup, the membrane voltage of the neuron was acquired

from a Brownlee Precision 440 amplifier (Brownlee Precision, San Jose, CA) by a National Instruments 6052E multifunction data acquisition board (National Instruments, Austin, TX) and used by the MRCI system to generate ionic currents, as shown in Figure 1. The current resulting from the conductance calculations was injected into the cell through the Axoclamp-2B in real time, creating a feedback system. This allows one to generate computational synaptic currents, as if they were in parallel with the neuron's intrinsic currents.

In addition to synaptic current generation, the dynamic clamp system was also used to capture experimental data. The spike times of action potentials were recorded using a threshold detection scheme, while the stimulus time was recorded as the beginning of the stimulus waveform. The spike time and stimulus time logs were faster and easier to process post hoc than the entire voltage and current waveforms recorded by the Clamp-Ex software.

Though the dynamic clamp technique has significantly contributed to our understanding of individual neurons and networks of neurons, the method has several limitations. As with current and voltage clamping techniques, the accuracy of the dynamic clamp is limited by the constraints of injecting current and recording voltage with the same electrode. The resistance and capacitance of the electrode cause measurement error and transient artifacts in the measured voltage. Techniques to minimize these artifacts have been developed, however they are imperfect. Inexact electrode compensation, either over-compensation or under-compensation, causes an error in the voltage measurement used by the dynamic clamp to solve computational

models of conductances. In addition, microelectrode capacitance and capacitance in the amplifier electronics causes transient artifacts and affects the time course of the system.

Another major limitation of the dynamic clamp technique is the sample and hold effect of the digital system. The dynamic clamp must sample the membrane voltage periodically, and use this to solve the conductance equations being simulated in real time. The computation time and dynamic clamp system overhead create a latency within the closed loop system. This delay limits the maximum sampling rate of the dynamic clamp system, which limits the accuracy and temporal dynamics of the simulation. The amount of delay needed is determined both by the complexity of the model being simulated and by the hardware platform the dynamic clamp is running on. A variety of dynamic clamp sampling rates were used to test the effect of latency on stability. Unless otherwise noted, the data shown in this paper was obtained with the MRCI system running at 10 kHz, or a latency of .1 ms.

The effects of the properties of the voltage dependent state variables, time delay, and measurement noise on numerical solution accuracy has previously been examined (Butera and McCarthy 2004). In this aim, we focus on stability. In dynamic clamp experiments, as the magnitude of simulated ionic currents is increased, transient instabilities appear. As this magnitude is further increased, the system becomes totally unstable. The instability is not caused by quantization error or saturation in the electronic equipment. It is affected by the sampling rate of the dynamic clamp system, the compensation of the series microelectrode resistance, capacitance in the electrode and electronics, and the magnitude of the feedback (set by the conductance of the current).

The instability we have observed experimentally has also been reported through personal communication by other electrophysiologists. Exploring its causes will lead to insight into how to increase the utility of the dynamic clamp by increasing the range of currents it can simulate. In addition, it will provide insight into the most important considerations for dynamic clamp design. Dynamic clamp development is ongoing, with system development and support spread among multiple systems developed by independent labs. Insight into which parameters are important for making a more stable system will help guide this design process. For example, dynamic clamp sampling rates are currently set to ensure the desired temporal dynamics can be simulated; however, our research indicates that the sampling rate also significantly affects the stability of the system.

1.3.3 Phase Response Curves

One of the fundamental techniques used throughout this project is the phase response curve (PRC). A phase model is a limit cycle oscillator model commonly used in theoretical studies of all types of oscillating systems (Kiss et al. 2002; Kozyreff et al. 2000; Pantaleone 1998; Wiesenfeld et al. 1996). This type of model describes an oscillation about a limit cycle as:

$$\frac{d\theta_i}{dt} = \omega_i + H(\theta_i, \theta_j), \quad (1)$$

where θ is the phase of the oscillator along the periodic limit cycle, ω_i is its intrinsic frequency, and H describes how it responds to stimuli. H is commonly called the PRC (Glass and Mackey 1988). It is a measure of the change in phase caused by a stimulus, as a function of the phase of oscillator i and the stimulus oscillator j .

Methods

Measuring PRCs experimentally is a straightforward process. The neuronal oscillator is viewed as a phase model, with each action potential corresponding to a phase of zero. A stimulus is applied to the neuron a specific amount of time, t_s , after the action potential is detected. The stimulus will cause the succeeding action potential to fire either sooner, known as phase advance, or later, called phase delay. Voltage traces showing a phase delay caused by an inhibitory stimulus current are shown in Figure 2.

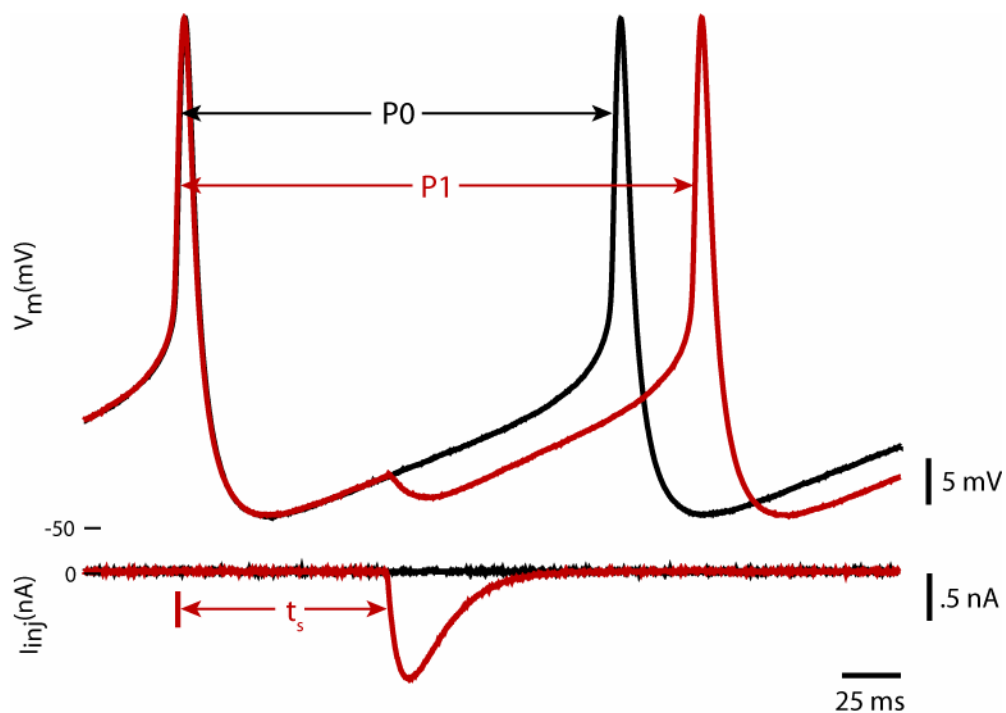


Figure 2. The effect of a perturbation on spike timing. In this example, a negative or inhibitory stimulus given to the neuron (red) at time t_s causes the subsequent action potential to fire later than it would in the unperturbed case (black).

To obtain a phase response curve, the period including the stimulus, P_1 , is measured and normalized by the unperturbed period, P_0 , to obtain the normalized phase change. This is subtracted from one, so that the phase change is a measure of the phase advance, i.e. negative phase changes are delays. The normalized phase change is plotted against the normalized phase where the stimulus was applied, t_s/P_0 , as one point on the

phase response curve. This process is repeated for a variety of stimulus times that sweep through the entire period of the neuron. An example PRC is shown in Figure 3.

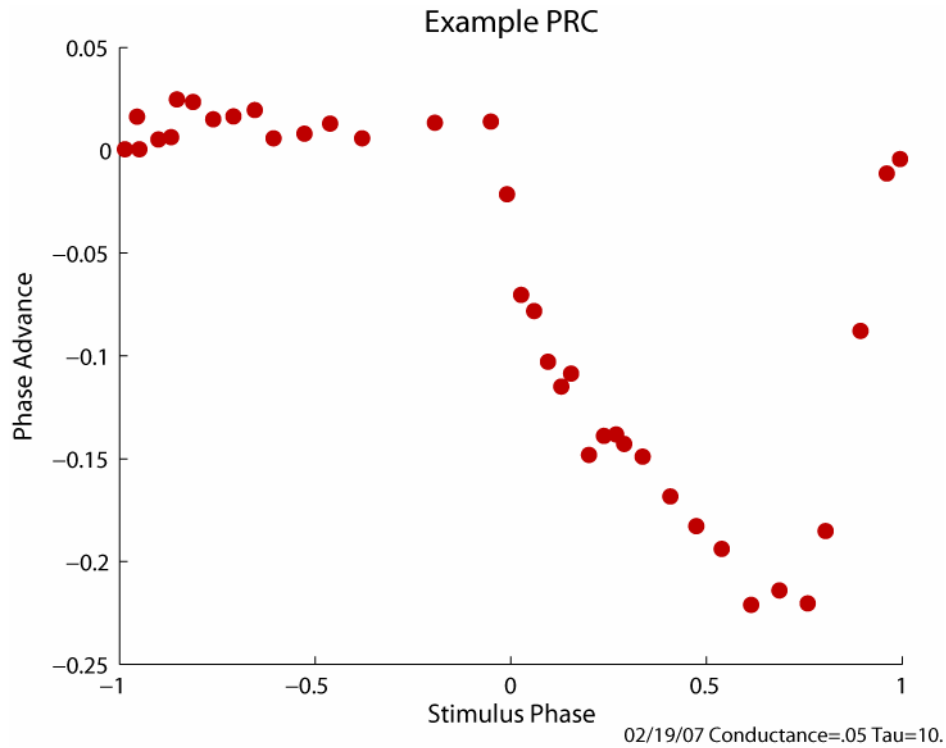


Figure 3. Phase Response Curve. This is an example of a PRC for an inhibitory stimulus with a synaptic time constant of 10 ms and maximal conductance of .05 μ s. Each point corresponds to one trial of applying the stimulus and measuring the resulting phase response. Negative phases correspond to the phase change that results from the stimulus being applied in the period before the period being measured.

It has recently been observed that the utility of PRC theory is extended if one considers second-order phase resetting (Oprisan et al. 2004; Preyer and Butera 2005), i.e. the effects of a stimulus on the cycle after the one in which it is applied. Such extensions seem evident when one considers the effect of non-pulsatile input that arrives toward the end of a cycle. If the stimulus phase is measured from the beginning of the stimulus, then the tail of the stimulus can extend into the subsequent period. Our analysis incorporates these effects as “negative phase” in our PRCs. Every stimulus is represented by two points on the PRC, a positive phase point describing the effect of the stimulus on the

current cycle, and a negative phase point, representing the effect of the stimulus on the next cycle.

1.3.4 Weak Coupling

Reducing the dynamics of spiking neurons to be functions of phase, also known as phase reduction, is employed in computational models of many types of oscillating systems, including Josephson junctions (Wiesenfeld et al. 1996), semiconductor laser arrays (Kozyreff et al. 2000), populations of chemical oscillators (Kiss et al. 2002), neutrino flavor oscillations (Pantaleone 1998), and neuron dynamics (Brown et al. 2004; Ermentrout 1996; Ermentrout and Kopell 1990b; Hansel et al. 1993; 1995; Pfeuty et al. 2005; Van Vreeswijk et al. 1994). Each of these theoretical studies uses phase reduction and the assumption that interactions between oscillators obey the weak coupling assumption. There are two levels of weak coupling, geometrically weak, which was first proposed by Winfree (Winfree 1967), and mathematically weak, which imposes a more stringent set of conditions. Throughout this paper, weak coupling will refer to the more stringent mathematically weak coupling that is a basic assumption in a significant number of computational studies. This form of weak coupling assumes that the response of a phase oscillator is the convolution of an intrinsic response function, often called an infinitesimal phase response curve (IPRC), with the applied stimulus function. This ability to separate the stimulus from the response is an extremely powerful assumption. It allows one to reduce a network model of phase oscillators to a system of variables representing phase differences. This simplified form provides the advantages of being both analytically solvable and significantly simpler than more complex models, allowing large network simulations to be done efficiently.

When using the weak coupling assumption, as initially described by Winfree (Winfree 1967), the PRC model, $H(\theta_i, \theta_j)$, in Equation 1 becomes:

$$H(\phi) = \int Z(\psi + \phi)S(\psi)d\psi, \quad (2)$$

where H is the oscillator's PRC, ϕ is the phase difference between the oscillator and the stimulus, Z describes the oscillator's IPRC as a function of the phase of the oscillator, and S is the stimulus waveform as a function of phase (Kuramoto 1984; Strogatz 2000). This assumption is based on the ideas that the oscillator is on a strongly attracting limit cycle and that the stimuli are weak and do not perturb it far from its limit cycle. As a result, the weak coupling assumption neglects amplitude effects caused by stimuli. Though it is frequently used, the assumption has not been previously verified in live neurons.

1.3.5 Coupling and Synchrony in Inhibitory Networks

Synchronous activity in inhibitory networks of neurons is found throughout the nervous system. It has been implicated in behavior, cognition, and memory (Buzsaki 1986; Gray 1994; Llinas and Ribary 1993). Theoretical and computational work predicts that identical neurons coupled together with mutually inhibitory synapses will exhibit anti-phase synchrony for fast synaptic rates and in-phase synchrony for slow synaptic rates (Ermentrout 1996; Hansel et al. 1993; 1995; Van Vreeswijk et al. 1994). Most of this existing computational work relies on simplified phase models of neurons, which use either spike time response (STR) methods or PRC methods to predict the modes of synchrony and phase locking that will result in a network of neurons. These methods are based on how an input to a neuron will advance or delay the future spikes of the neuron. Phase model methods are significantly simpler than detailed biophysical models. They

allow for simpler theoretical analysis and prediction of network behavior (Canavier et al. 1997; Dror et al. 1999; Ermentrout 1996; Ermentrout and Kopell 1991; Hansel et al. 1993; 1995; Skinner et al. 1994; Terman et al. 1998; Van Vreeswijk et al. 1994; Wang and Buzsaki 1996; Wang and Rinzel 1992). In one theoretical study, Van Vreeswijk, Abbott and Ermentrout (1994) use general phase-coupled models and Hodgkin-Huxley style models to demonstrate the stable phase locked solutions that result when the synaptic time constant between two identical coupled neurons is increased. For inhibitory synaptic coupling, they show an abrupt change from anti-phase to in-phase synchrony as the synaptic time constant is increased. Figure 4 shows their results for inhibitory coupling of two identical Hodgkin-Huxley style neurons coupled with alpha-shaped synapses. This figure shows that for fast synaptic rates (large α) coupled neurons exhibit anti-phase synchrony, locking with a phase difference of 0.5. As α is reduced, there is a region of bistability, where both the in-phase ($\varphi = 1.0$) and the anti-phase solutions ($\varphi = 0.5$) are stable. Finally, for slow synaptic rates (small α), only the in-phase solution is stable.

Many of the above studies use identical oscillators to examine phase locking and synchrony in coupled oscillators. In biology, however, there is always some degree of heterogeneity in networks of neurons. When small levels of heterogeneity are added to the firing frequency of the coupled oscillators, differences of greater than a few percent of intrinsic firing frequency dramatically reduce the synchronous firing region for slow synaptic time constants (Skinner et al. 2005; White et al. 1998). Other coupling experiments that include firing frequency heterogeneity in networks of two coupled Wang and Buzsaki neurons show bistability between in-phase synchrony and anti-phase

synchrony for time constants of 1/10th of the firing period. When heterogeneity is increased, however, the anti-phase solution is lost even for short time constants (Maran and Canavier 2007; Wang and Buzsaki 1996).

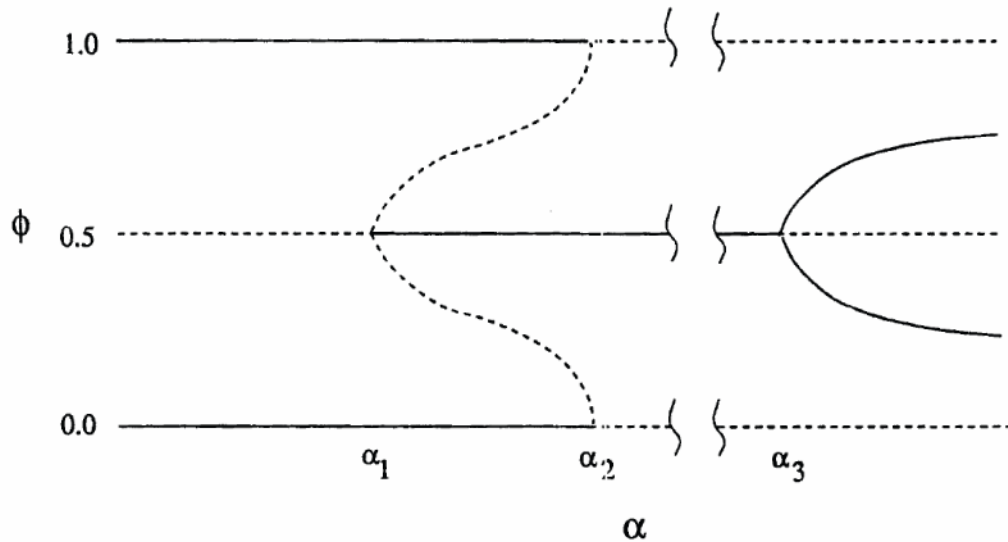


Figure 4. Phase differences of phase locked solutions for two identical Hodgkin-Huxley oscillators as a function of synaptic rate. Solid lines are stable solutions, while dotted lines are unstable solutions. For large α , i.e. fast synapses, the anti-phase solution is stable. As the coupling rate is reduced, the in-phase solution becomes stable as well. Finally, for slow synapses, only the in-phase solution is stable. Taken from Figure 8 of Van Vreeswijk, Abbott, and Ermentrout (Van Vreeswijk et al. 1994).

There have been a few attempts to verify these computational results using live neurons. Elson et al. (2002) used bursting neurons to show both anti-phase synchrony and in-phase synchrony as the synaptic coupling time constant was increased. Their results show it is possible to obtain both modes of synchrony depending on the synaptic time constant; however, most computational literature involves tonically firing neurons, and not bursting ones (Elson et al. 2002). Merriam et al. (2005) show bistability in networks of tonically firing neurons from the auditory cortex. They show that as the synaptic time constant for coupling between two inhibitory neurons is increased, the network goes from

predominantly anti-phase synchrony to a bistable system with both in-phase and anti-phase stable solutions. Their results do not show phase locking; instead, their conclusions are based on histograms showing the predominant phase differences between the coupled neurons (Merriam et al. 2005). Finally, Netoff et al. (2005) show both the anti-phase and in-phase synchronous modes as the synaptic time constant is increased in networks of coupled neurons and hybrid networks of one live neuron and one model neuron (Netoff et al. 2005b). In their results, they predominantly observe the anti-phase solution, unless the synaptic time constant is very large. To obtain these results, they use a constant background current to maintain the firing frequency of the live neurons. This current is adjusted every few cycles to ensure the firing frequency does not change. It is easy to show, however, that the network frequency of two coupled oscillators changes with coupling. As a result, maintaining a constant firing frequency for the neurons may alter the natural behavior of the coupled network.

CHAPTER 2

WEAK COUPLING

The first aim of this research was to validate the assumption of weak coupling using live neurons. As mentioned in the introduction, the weak coupling assumption is commonly used in computational modeling of oscillatory systems, including networks of coupled neurons. Until this research, however, the assumption had not been experimentally validated. This chapter proves that the weak coupling assumption is valid for invertebrate neurons in the abdominal ganglia of *Aplysia californica*. We applied weak stimuli to neuronal oscillators and deconvolved the IPRCs described in the Weak Coupling section of Chapter 1. Here we show that these IPRCs reliably predict the phase response for weak stimuli, independent of the stimulus waveform used. These weak stimuli are in the range of normal synaptic input for these neurons, suggesting that weak coupling is a likely mechanism.

2.1 Methods

The weak coupling assumption states that the phase response of an oscillator is the convolution of the stimulus and the IPRC, as shown in Equation 2 of Section 1.3.4 Weak Coupling. For this to be true, the PRC amplitude should scale linearly with stimulus amplitude but be shape invariant, because convolution is a linear function. In addition, the IPRCs should predict the phase response of a neuron to any stimuli, independent of the stimulus waveform used to generate the IPRC. This section begins by demonstrating the linear relationship between the PRC and stimulus amplitude. We then

obtain IPRCs from PRCs and measure their ability to predict the phase response of a neuron.

2.1.1 Linear Scaling

The first step in demonstrating mathematically weak coupling as defined by Winfree (Winfree 1967) was to show that small stimuli PRCs scale linearly with stimulus magnitude. To test this theory, PRCs were measured in response to a wide range of stimulus amplitudes. These PRCs are shown in Figure 5A and Figure 5B. These stimuli range from just barely affecting the neuron, where the PRC looks like noise, to stimulus strengths that automatically trigger an action potential, where the PRC appears to be linear. We then took each PRC data point and scaled it to a common maximal conductance. This was done by multiplying the magnitude of the phase change, by the common maximal conductance divided by the stimulus magnitude. The weak stimuli PRCs were scaled to a common maximal conductance of $.1 \mu\text{S}$, while the strong stimuli PRCs were scaled to $.6 \mu\text{S}$. Figure 5C and Figure 5D show the results of this scaling experiment. For weak stimuli, Figure 5C, the scaled PRCs are identical, meaning they scale linearly. For strong stimuli, Figure 5D, the curves have different shapes, indicating that they do not scale linearly. While linear scaling is necessary for mathematically weak coupling, it is not a sufficient proof of its existence.

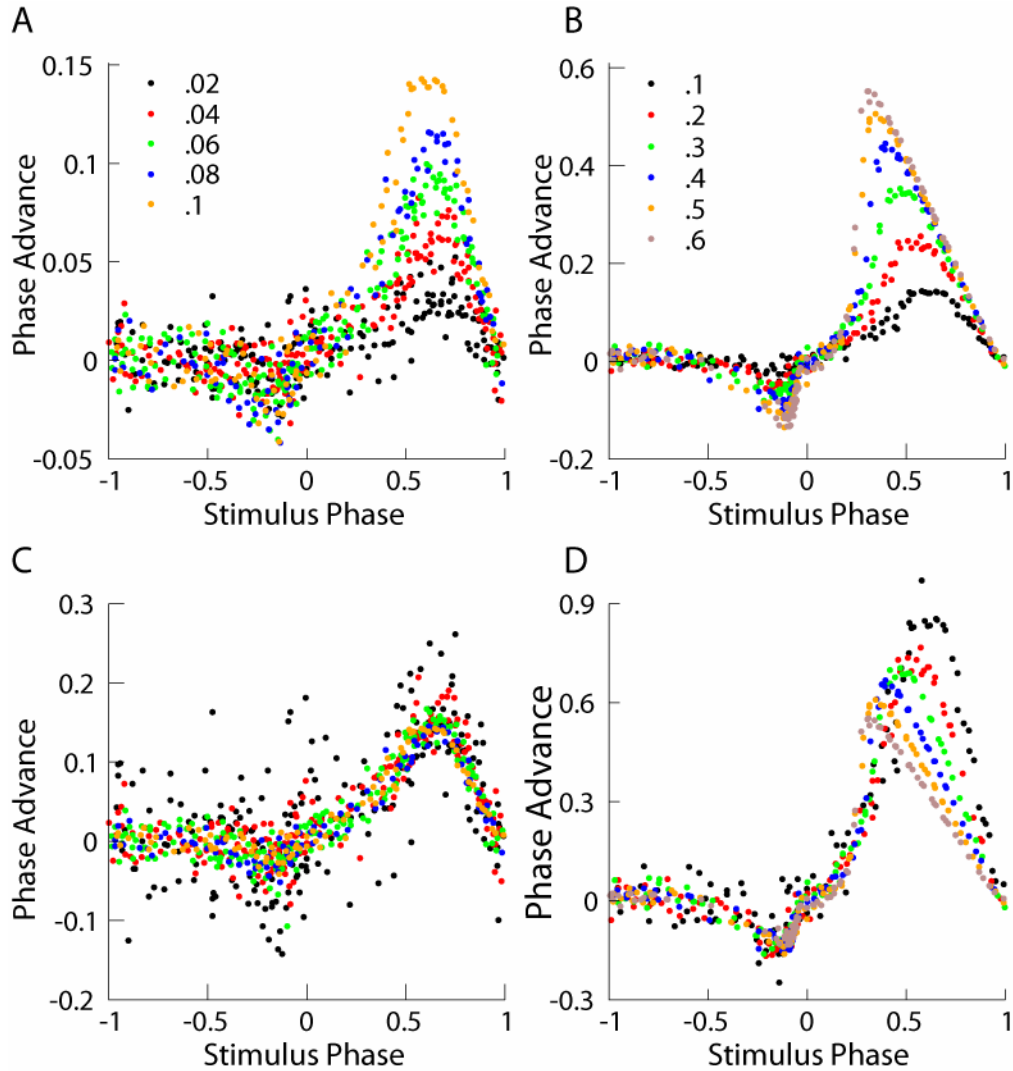


Figure 5. Linear scaling of PRCs. Weak amplitude stimuli elicit PRCs that scale linearly with amplitude, while large stimuli do not. PRCs were obtained from the same neuron for a wide range of stimulus amplitudes, for $\tau = 10$ ms. Cobalt chloride saline was used to eliminate synaptic input. (A) Weak stimuli PRCs measured for conductances ranging from $0.02 \mu\text{S}$ – $0.1 \mu\text{S}$. (B) Strong stimuli PRCs for conductances from $0.1 \mu\text{S}$ – $0.6 \mu\text{S}$. (C) Weak stimuli PRCs scaled, point by point, to a conductance of $0.1 \mu\text{S}$. (D) Strong stimuli PRCs scaled to a conductance of $0.6 \mu\text{S}$.

2.1.2 IPRCs

To further validate the weak coupling assumption, *in vitro*, we obtained IPRCs for different stimulus shapes and used them to predict the phase response of that neuron to a different stimulus. For this experiment, three different stimulus waveforms were used to generate PRCs from each neuron. The stimuli were alpha-shaped conductances with a

time constants, τ , of 10, 20, and 40 ms, as shown in Figure 6A. The resulting PRCs are shown in Figure 6B. Conductances were scaled by a maximal conductance, g , and the time constant, τ , so that the amount of injected conductance was equal across all three stimuli, as shown in Equation 3:

$$I_{syn} = g_{syn} \alpha(t) \frac{e}{\tau} (V_m - E_{syn}), \quad (3)$$

$$\frac{d\alpha}{dt} = \frac{-\alpha}{\tau} + y, \quad (4)$$

$$\frac{dy}{dt} = \frac{-y}{\tau} + trig. \quad (5)$$

Each PRC in the set of three was then spline fit to remove experimental noise, and the stimulus waveform was deconvolved from the spline fit to obtain the IPRC. Performing straight deconvolution often led to numerical instability, so we used a minimization algorithm to obtain our IPRCs. With this algorithm, we assumed the IPRC was a 10th order polynomial and found the coefficients that minimized the mean squared error (MSE) between the spline fit PRC and the polynomial IPRC convolved with the stimulus waveform used to generate the PRC. Some examples of the resulting IPRCs are shown in Figure 7A-C.

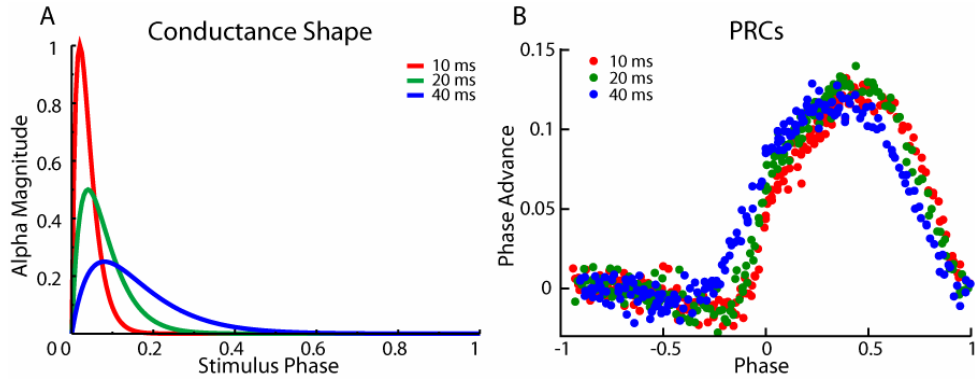


Figure 6. Conductances and PRCs. (A) Shows the conductance traces used to generate the stimulus current. (B) Example PRCs generated with the conductance waveforms shown in A.

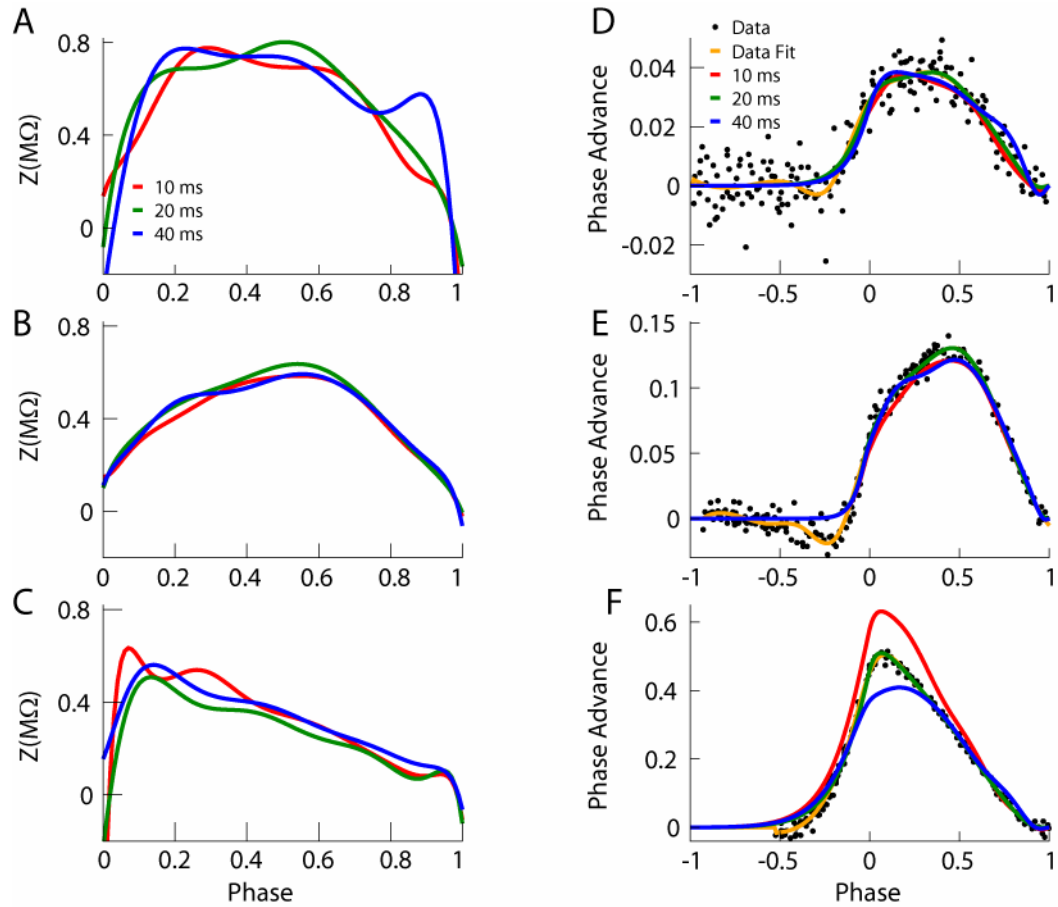


Figure 7. IPRCs and reconstructed PRCs. The IPRCs and reconstructed PRCs for 3 different experiments. (A) - (C) Each panel shows three IPRCs recovered for stimuli with $\tau = 10, 20,$ and 40 ms. (D)-(F) The IPRCs convolved with stimulus waveforms are better able to reproduce PRC data for weak amplitude stimuli. Data points are the measured PRCs in response to stimuli with $\tau = 20$ ms. The orange trace is a spline fit to the PRC data points, red, green, and blue traces are the convolution of the IPRCs shown in panels A-C with the $\tau = 20$ ms stimulus waveform. The rows correspond to different experiments with increasing stimulus strengths. The set conductance, g , and maximum PRC amplitude of 10 ms PRC, $\Delta\theta$, are (A, D) $g = 0.005 \mu\text{S}$, $\Delta\theta = 0.038$; (B, E) $g = 0.04 \mu\text{S}$, $\Delta\theta = 0.095$; (C, F) $g = 0.12 \mu\text{S}$, $\Delta\theta = 0.694$.

For weak coupling to be valid, the IPRCs from each neuron must be able to predict the phase response that neuron would have to a different stimulus. To test this, each IPRC was convolved with each of the three stimulus waveforms in the set. For example, the 20 ms stimulus waveform was convolved with the 10, 20, and 40 ms IPRCs. The resulting waveforms were compared to the original 20 ms PRC, as shown in Figure

7D-F. To quantify our results, the MSE between the reconvolved waveform and the spline fit of the experimental data was tabulated (Table 1). We found that for all experimental datasets, the MSE was a very good indicator of the quality of the fit of the reconvolved PRC. This can be observed by comparing the fits in Figure 7D-F with the data in Table 1.

Table 1. MSE results for the three experiments in Figure 7. The values represent the MSE between the PRC data (τ in rows) and the convolution of the IPRC (τ in columns) and the stimulus waveform (τ in rows). Values in brackets are powers of ten. Experiments correspond to increasing stimulus strength, and are for a set conductance, g , and maximum PRC amplitude of the 10 ms PRC, $\Delta\theta$, of (a) $g = 0.005 \mu\text{S}$, $\Delta\theta = 0.038$; (b) $g = 0.04 \mu\text{S}$, $\Delta\theta = 0.095$; (c) $g = 0.12 \mu\text{S}$, $\Delta\theta = 0.694$.

Expt	Stim τ	IPRC		
		10	20	40
a	10	3.2 [-6]	7.7 [-6]	1.7 [-5]
	20	4.9 [-6]	2.4 [-6]	7.1 [-6]
	40	5.2 [-6]	3.3 [-6]	1.9 [-6]
b	10	4.0 [-5]	6.1 [-5]	5.0 [-5]
	20	5.6 [-5]	3.4 [-5]	4.8 [-5]
	30	2.3 [-5]	2.7 [-5]	1.7 [-5]
c	10	4.8 [-4]	3.6 [-6]	9.0 [-3]
	20	4.6 [-3]	1.6 [-4]	1.6 [-3]
	40	5.9 [-3]	5.5 [-4]	5.6 [-5]

2.2 Results

2.2.1 Linear Scaling

As Figure 5 indicates, there is a linear scaling relationship in PRCs generated from weak stimuli. This is visually apparent in scaled versions of the PRCs, where each point is scaled, by multiplication, to a common maximal conductance. For small stimuli PRCs, these scaled PRCs appear to be identical in shape. The smallest stimuli PRCs have more noise, which is a result of experimental noise that is amplified by scaling. This linear scaling does not hold true for strong stimuli. In this case, scaled PRCs have a

different basic shape, indicating that there is a non-linear relationship between the strong stimuli and the PRC.

2.2.2 IPRCs

To quantify how well the IPRCs could predict the neuronal phase response to different stimuli across experiments with different neurons, we needed an accurate measure of stimulus strength that was independent of the intrinsic neuronal properties. We chose the maximum amplitude of the PRC as a measure of how strongly the neuron was affected by a stimulus, in lieu of pure stimulus amplitude, to account for variability among the input impedances of different neurons. Figure 8 illustrates the MSE between the spline fit of the PRC data and the predicted PRC (convolution of IPRC and stimulus) as a function of the maximal PRC amplitude for all experimental sets (n=36 sets, from 12 different neurons). Panels A-C correspond to different stimulus PRCs, while the data point's color represents the IPRC used in the convolution. At the lower PRC amplitudes, the MSE decreases by several orders of magnitude. Thus, the convolution integral reliably reproduces the neuronal response for weak stimulus strengths, but not strong ones. This weak range includes values that are similar to the normal synaptic input seen by these cells. Similar trends in results were obtained when using the R^2 metric to measure error.

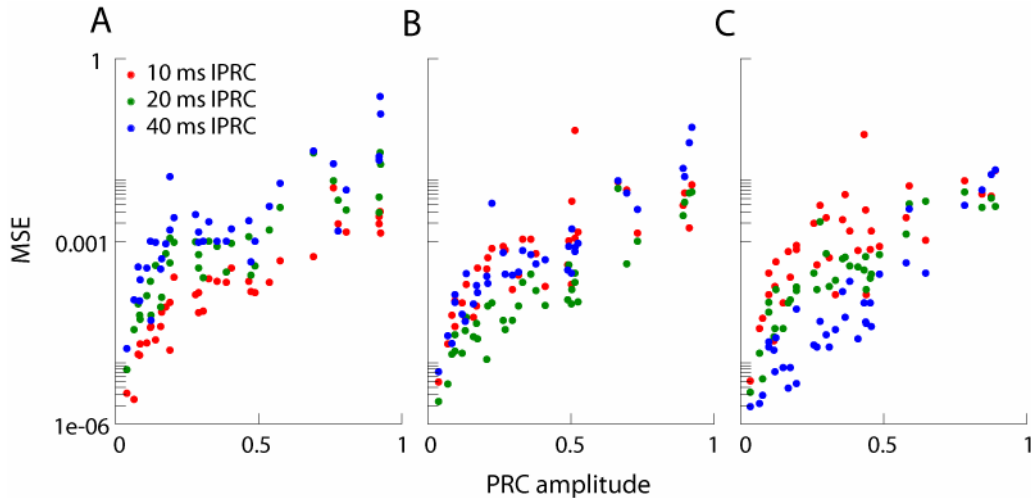


Figure 8. There is a several order-of-magnitude reduction in MSE for low amplitude PRCs. MSE is plotted as a function of PRC amplitude across all experiments. Red, green, and blue points represent MSEs between the experimental PRC data and the reconvolved PRCs for IPRCs in response to $\tau = 10, 20,$ or 40 ms stimuli, respectively. IPRCs are convolved with stimulus waveforms and compared to the spline fit PRC data. Panels correspond to stimulus waveforms. (A) $\tau = 10$ ms stimulus. (B) $\tau = 20$ ms stimulus. (C) $\tau = 40$ ms stimulus.

2.3 Discussion

Prior to blocking synaptic activity in these neurons, the typical postsynaptic potentials have amplitudes from 2.5 to 15 mV and do not trigger an action potential. We quantified the amplitude of the voltage deflection in response to our stimuli applied at a phase of approximately 0.3. Of those stimuli that did not elicit action potentials, 75% produced deflections of 1 to 20 mV, with the remainder producing larger deflections up to 40 mV. The stimuli that did elicit action potentials correspond to PRC amplitudes of 0.5 or larger in Figure 8. This indicates that not only is weak coupling a valid assumption to make theoretically, but that it is within the normal range of operation of the neuron. As such, it is a likely mechanism for coupling in these neurons.

Demonstrating that the weak coupling assumption holds in neurons benefits both theorists and biologists. Theorists already commonly use this assumption in computational simulations and analytical solutions. Demonstrating it *in vitro* validates

their use of the assumption. Biologists currently measure PRCs as a way to quantify the behavior of a neuron without needing to understand the underlying mechanisms; however, they do not take advantage of the weak coupling assumption. PRCs have been measured and used in maps to predict synchronization in hybrid systems (Merriam et al. 2005; Netoff et al. 2005b; Oprisan et al. 2004), but these methods require a PRC for each stimulus used. Weak coupling can facilitate realistic experiments that include different stimulus shapes and multiple inputs per cycle, without requiring a PRC for each stimulus scenario used.

Other researchers have already demonstrated that experimentally obtained PRCs predict situations of entrainment or synchronization (Netoff et al. 2005b; Oprisan et al. 2004; Perkel et al. 1964). Their methods did not assume weak coupling; they used a more general type of PRC theory that relies upon maps of the pre-stimulus to post-stimulus phase. Such approaches are severely limited by the fact that the measured PRC is valid only for the specific stimulus waveform used. Other approaches deconvolve input stimuli from output measures to obtain a “kernel” that describes the input-output transformation. This has been applied in several areas of neuroscience to describe stimulus-response experiments. For example, Poliakov et al. showed that Wiener kernels could be used to describe how input to a motoneuron was transformed into a time series of output spikes characterized by a peri-stimulus time histogram (Poliakov et al. 1997). Our method is primarily different from these in that we are studying effects upon a single limit cycle oscillation, while most stimulus-response studies using kernel-based methods typically study longer-term aggregate measures of neural activity that span multiple limit cycles.

Though several groups have measured PRCs from oscillatory excitable cells, and many theorists make the weak coupling assumption in their models, we are aware of only two attempts to deconvolve IPRCs. Galán et al. implicitly fit the IPRC as part of a PRC estimation procedure, while Netoff et al. use IPRCs to predict the synchronization of coupled oscillators with multiple synaptic inputs (Galan et al.; Netoff et al. 2005a). Though these papers implicitly assume weak coupling by calculating IPRCs, neither attempts to systematically validate how consistent the derived IPRCs are with weak coupling assumptions. For example, Netoff et al. calculate IPRCs in response to different stimuli. The IPRCs are similar in general shape, but the amplitude and alignment of the deconvolved IPRCs, obtained from the same cell, are noticeably different (Netoff et al. 2005a).

We have successfully demonstrated that there is a large range of stimulus strengths where an IPRC can be deconvolved from the PRC of a neuron and the applied stimulus. This function accurately reproduces the phase response of the neuron to other stimulus shapes. The range where this is possible includes coupling strengths comparable to synaptic events seen in these neurons *in vitro*. These results are the first to demonstrate that such assumptions may be realistic in specific cases. This evidence supports assumptions made in phase reduction modeling, which require weak coupling within networks of oscillators to simplify the systems so network behavior can be studied.

CHAPTER 3

COUPLING AND PHASE RESPONSE CURVES

The weak coupling assumption and other phase model methods have been used to computationally predict which modes of synchrony will exist for networks of coupled neurons. These studies are based on phase models that describe how subsequent firing of a neuron is affected by a stimulus. All of these studies predict that two identical neurons coupled together with fast inhibitory synaptic coupling will exhibit in-phase synchrony. As the synaptic time constant is lengthened, there is a region of bistability, where both an in-phase solution and an anti-phase solution are stable. Finally, for slow synaptic coupling, the only stable phase locked mode is in-phase. When small amounts of heterogeneity are added, these coupled networks exhibit near in-phase and near anti-phase synchrony, but as heterogeneity is increased the anti-phase solution is lost, even for fast synaptic time constants.

Experimental verification of these results is difficult for a number of reasons. The heterogeneity present in real neurons makes it extremely difficult to obtain phase locked coupling under controllable study conditions. Any variability in the firing rate of the neuron makes it difficult to find phase locking. As a consequence, previously published experiments have only qualitatively verified that both anti-phase synchrony and in-phase synchrony can be observed, and that there are regions of bistability between these two extremes. This work is the first to thoroughly examine how well PRCs are able to predict phase locking and explore how the transition from anti-phase to in-phase synchrony occurs. Computational theory indicates that there is an abrupt transition from anti-phase

synchrony to in-phase synchrony, with a small range of bistability; however, our experiments show that the transition is, in fact, gradual.

Our invertebrate experimental preparation is an ideal candidate for studying PRC predictions and the transitions between anti-phase and in-phase synchrony. Our neurons fire extremely regularly, eliminating the need for external control of the firing frequency. These neurons fire with less variability than other experimental preparations used to study coupling behavior, allowing us to measure phase differences more accurately than previous results obtained from cortical neurons (Merriam et al. 2005; Netoff et al. 2005a).

In Aim 2, we use the dynamic clamp to create inhibitory networks of two neurons. These networks are hybrid networks consisting of one live neuron from the abdominal ganglia of *Aplysia californica* and one Wang and Buzsaki model neuron (Wang and Buzsaki 1996). Using alpha-shaped inhibitory synaptic conductances, we investigate the phase-locking behavior of this network as the synaptic rate is varied. We confirm the anti-phase and in-phase synchrony predicted by computational literature, with an intermediate region of bistability. Analytical solutions obtained from PRCs correctly predict stable phase locked solutions observed in experimental coupling results. We also show that phase models created with experimental PRCs show the same trends that the analytical solutions and the experimental coupling results show. Finally, unlike the previous computational predictions made with phase models, we show a gradual transition from anti-phase to in-phase synchrony as the synaptic time constant is increased. This transition is present in predictions from the PRC based models and the existence and stability criteria described in Oprisan et al. (2004) (Dror et al. 1999; Oprisan et al. 2004).

3.1 Methods

This work is divided into two sets of experiments. In the first section, we create a hybrid inhibitory network of one live neuron and one Wang and Buzsaki neuron using computational synapses created with the dynamic clamp system. Using different time constants for the synaptic coupling we examine how phase locking changes as a function of the synaptic time constant. The second part of this work uses PRCs obtained from the same neurons to predict the existence of phase locked solutions. We then compare these to the phase-locked results observed experimentally.

3.1.1 Computational Models

For these experiments, the dynamic clamp was used to implement both computational synapses between neurons and the computational Wang and Buzsaki model neurons.

Computational Synapses

Hybrid networks of neurons were created by implementing computational synapses between uncoupled neurons using the MRCI dynamic clamp system. These synapses were based on an alpha-shaped synaptic conductance, allowing us to control the synaptic rate with only one time constant. Equations 6-8 were used to implement this conductance waveform:

$$\frac{dy}{dt} = \frac{-y}{\tau} + trig, \quad (6)$$

$$\frac{d\alpha}{dt} = \frac{-\alpha}{\tau} + y, \quad (7)$$

$$I_{syn} = g_{syn}(t)\alpha(t)\frac{e}{\tau}(V_m - E_{syn}). \quad (8)$$

In these equations, I_{syn} represents the total synaptic current injected into the post-synaptic neuron. This is a function of the maximal conductance, $g_{syn}(t)$, the synaptic waveform, $\alpha(t)$, and the driving force, $(V_m - E_{syn})$. The synaptic waveform, α , is normalized to a height of one by the e/τ term. It is activated by *trig*, a square pulse with an amplitude of 1 and a duration of 1 ms that is set when the pre-synaptic neuron crosses a threshold, indicating it has fired an action potential.

Wang and Buzsaki Model Neuron

We chose the Wang and Buzsaki computational model neuron because its PRCs are similar to the biological neurons being used. Appendix A describes the Wang and Buzsaki model and its equations. The spiking rate of the Wang and Buzsaki neuron was set to match the firing rate of the live neuron through the I_{app} parameter of the model.

Different input impedances among the cells of the hybrid networks forced us to match synaptic strengths based on the PRC amplitude, in lieu of the maximal conductance of the synaptic waveform. For this matching, a PRC was measured from the biological neuron using a synaptic time constant of 10 ms and the largest maximal conductance that did not cause the system to become unstable, see Chapter 4, Dynamic Clamp Stability. The matching synaptic strength for the Wang and Buzsaki model maximal synaptic conductance was found using a simulated model to generate matching PRCs. The maximal conductance that resulted in the same maximum PRC phase change was used to make the synaptic current injected into the Wang and Buzsaki model neuron in the coupled network. Matching was only performed for one time constant because the

PRCs scale similarly for small time constants. An example of matched PRCs is shown in Figure 9.

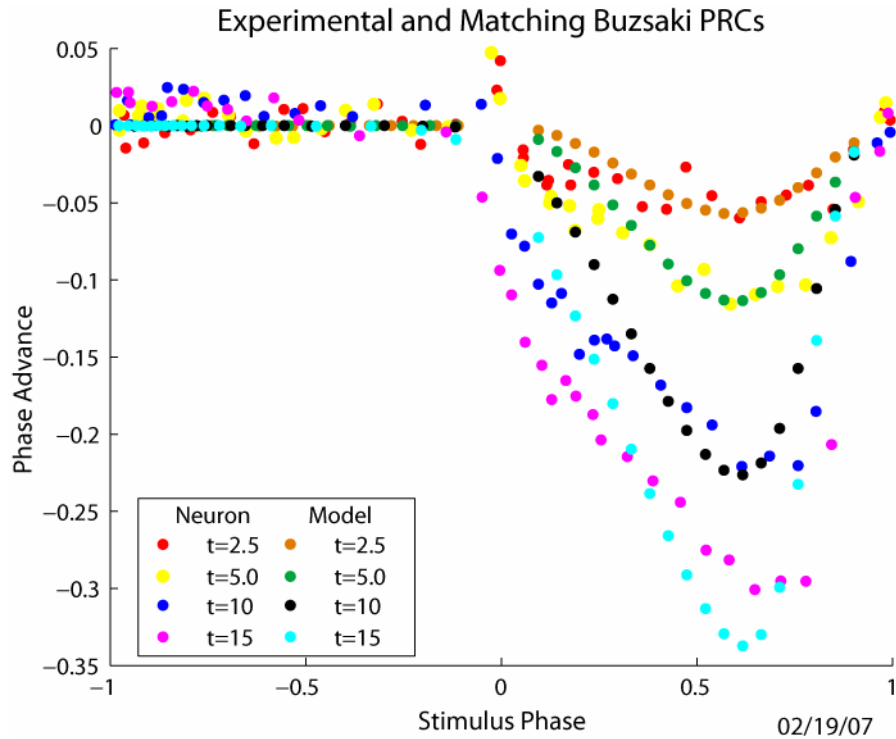


Figure 9. Matched PRCs from a live neuron and a Wang and Buzsaki model neuron. For small time constants the matched PRCs are similar. The live neuron g_{syn} is $.05 \mu S$, while the Wang and Buzsaki model's g_{syn} is $.0024 \mu S$.

3.1.2 Coupling Experiments

The goal of these experiments was to examine how the phase locking of the network changed as a function of the synaptic time constant. The dynamic clamp was used to create both artificial inhibitory synaptic coupling between neurons and to simulate the equations for the Wang and Buzsaki model neuron. Synaptic currents were triggered when the membrane voltage of the opposite neuron crossed a threshold, indicating an action potential had been fired.

We chose to change only the synaptic time constant, and not adjust the maximal conductance (not ensuring a constant amount of injected current). In experiments where

the maximal conductance was scaled with the synaptic time constant, we did not observe a significant difference in the measured PRCs. As a result, we chose to manipulate only the synaptic time constant for all experiments.

Two different protocols were used for the coupling experiments. The goal of preliminary coupling experiments was to show the anti-phase solution for fast time constants, the in-phase solution for slow time constants, and bistability between these regions. Once we determined this was possible, we switched to examining the transition from anti-phase to in-phase synchrony.

Preliminary Experiments

Preliminary coupling experiments were designed to explore not only phase locking, but also bistability. For each time constant examined, the synapses between neurons were turned on and off for 15-30 second intervals repeatedly to explore what types of phase locking resulted. This repetition was done to determine whether the two neurons would phase lock to different phases for different initial conditions. Turning the synapses on and off was more effective at finding multistable states than leaving them on and observing spontaneous mode switching. This is because some of the modes of synchrony, especially the in-phase solutions, were very stable. Experimental noise was not always sufficient to evoke mode switching in these cases, even though bistability was observed with multiple trials. The phase differences were recorded in raster plots and examined histograms, as explained in Section 3.1.5 Data Analysis.

Transition Experiments

Once we qualitatively determined that our coupled neurons phase locked in anti-phase synchrony for fast synapses and in-phase for slow synapses, with bistability in

between, we modified our coupling experiments to examine the transition from anti-phase to in-phase. Most of the data for this section was obtained by turning the synapses on for a given synaptic time constant and slowly incrementing the synaptic time constant in small steps every 1-3 minutes, without turning the synapses off. For larger synaptic time constants, the anti-phase solution appears to occur for a smaller range of initial conditions, and, as a result, is harder to obtain from the preliminary experiments alone. Starting from this solution allowed us to track how the anti-phase solution changes as the time constant was increased.

Plots from these transition experiments often contain a contiguous series of τ measurements taken without turning the synapses off. The plots also display larger time constants that were used to verify that the in-phase solution remained stable. Bistability was not examined in this section.

3.1.3 PRC Existence and Stability Criteria

PRCs were also measured from the live neurons and used to predict phase locked modes using the existence and stability criteria described by Dror et al. (1999) and Oprisan et al. (2004) (Dror et al. 1999; Oprisan et al. 2004). With this method, phase locked modes are obtained analytically from the PRC data. The existence and stability criteria are based on several key assumptions. First, each input received by the neuron must be independent, and the oscillator must return to the limit cycle oscillator before receiving another input. This allows PRCs generated using the open loop method, described in 1.3.3 Phase Response Curves, to predict the closed loop behavior of a coupled network. The second assumption is that the synaptic input received by the

neurons must be similar to the stimulus used to generate the PRC curve. For our experiments, these will be identical.

For phase-locked solutions to exist, both neurons must have the same period. In other words, the sum of the stimulus time (time from an action potential until an input is received from the other neuron) and recovery time (time from stimulus to next action potential) must be equal for both neurons (Canavier et al. 1999; Canavier et al. 1997; Luo et al. 2004). This definition is shown in Equation 9. The sum of the stimulus and recovery times are simply equal to the original period plus the amount of first and second order phase resetting, $F_{1,j}$ and $F_{2,j}$:

$$t_{s,1} + t_{r,1} = t_{s,2} + t_{r,2}, \quad (9)$$

$$t_{s,1} + t_{r,1} = P0_j (1 + F_{1,j}(\phi_j) + F_{2,j}(\phi_j)). \quad (10)$$

One can use these relationships to obtain steady state values for t_s and t_r , and find solutions that satisfy the periodicity criterion from Equation 9, as described in Oprisan et al. (2004).

The stability criterion, was first established by Dror et al. (1999) with first order phase resetting and expanded by Oprisan et al. (2004) to include second order effects (Dror et al. 1999; Oprisan et al. 2004). This criterion uses linearized discrete maps of successive phases to determine the slope of the PRC that will maintain a stable phase-locked relationship. This mapping requires the slopes of the PRCs to satisfy the characteristic equation

$$\lambda^2 - ((1 - m_{1,1})(1 - m_{1,2}) - m_{2,1} - m_{2,2})\lambda + m_{2,1}m_{2,2} = 0. \quad (11)$$

In this equation, $m_{1,1}$ is the slope of the first-order PRC for neuron 1 and $m_{2,1}$ is the slope of the second-order PRC for neuron 1. For a solution to be stable, the roots of this equation must be between -1 and 1. For this project, PRCs were analyzed for phase-locked solutions using code written by Dr. Carmen Canavier.

3.1.4 PRC Emulator

In addition to performing coupling experiments with live neurons, we used PRC measurements from the same neurons to predict network behavior. For these experiments, PRCs were measured from the neurons used for the coupling experiments described above, with the protocol described in Section 1.3.3 Phase Response Curves. Simulations of phase models based on these PRCs were used to predict the modes of synchrony for the synaptic time constants of the PRCs.

The first step in this process was to fit the experimental PRCs with a curve. It has been previously shown that in addition to first order phase resetting, the effect of a stimulus on the cycle it is applied to, it is also beneficial to include second order phase resetting, or the effect on the succeeding cycle (Oprisan et al. 2004; Preyer and Butera 2005). For our PRCs, these second-order effects are depicted at phases of -1 to 0, which are the phases that correspond to just before the current cycle. We used a cubic smoothing spline, the CSAPS algorithm in Matlab (The Mathworks, Natick, MA), with a smoothing parameter of .9997 to fit and smooth the data. This parameter was determined by visual inspection; it captured the shape of the PRC well, while smoothing the noise in the experimental data. Figure 10 contains examples of PRCs and their curve fits for both live neurons and the matching Wang and Buzsaki model neurons.

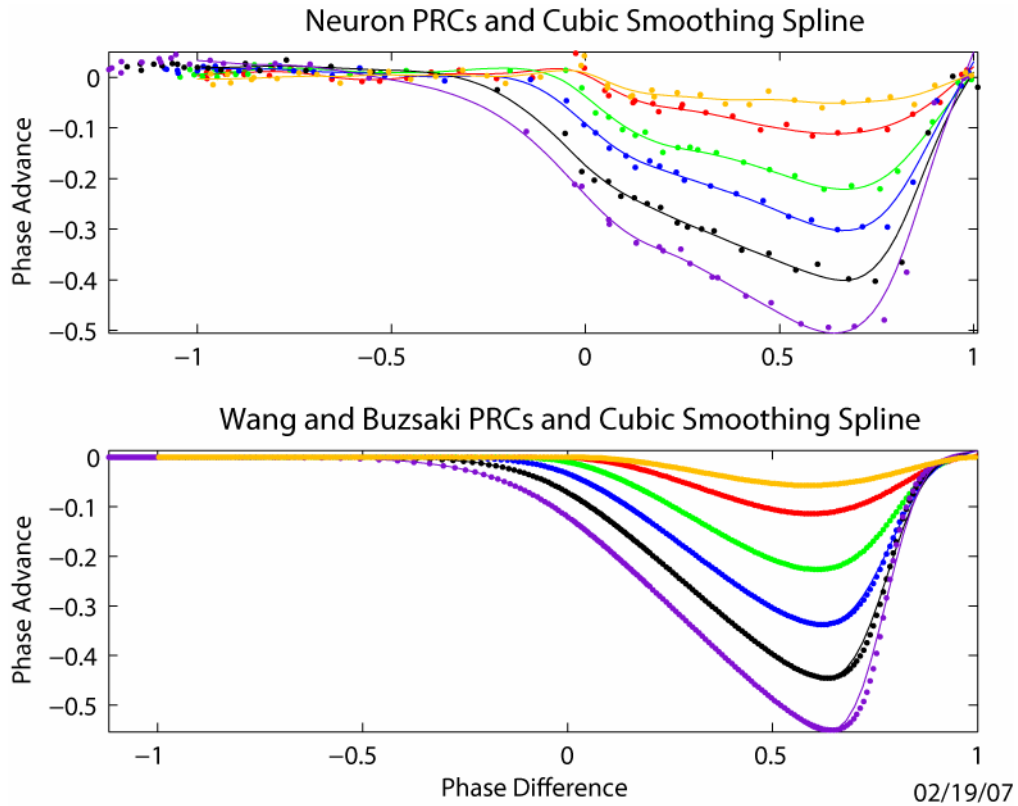


Figure 10. Data points are PRCs from a live neuron (top) and a Wang and Buzsaki model neuron (bottom) with the corresponding cubic smoothing spline curve fits.

Fits were obtained for both the experimentally measured neuron PRCs and the matched Wang and Buzsaki model PRCs. The resulting curve fits were used in a phase model simulator to predict what stable phase-locked solutions exist when the two phase oscillators are coupled together. Each phase oscillator was implemented as a phase counter counting from the reset phase (zero, when there is no second order resetting) to one. When the counter reaches one, the neuron fires an action potential and is reset to the reset phase, as shown in Figure 11. When a neuron fires an action potential, the first-order phase response is immediately applied to the other neuron. The amount of phase change is calculated from the spline fit of the appropriate PRC. The second-order phase response is implemented by changing the phase the postsynaptic neuron will be reset to when it fires the next action potential. In this way, second-order resetting is applied to the

next cycle. The simulator results were tallied in phase difference raster plots and histograms using the techniques described in Section 3.1.5 Data Analysis. The PRC phase model simulations for this project were completed using code provided by Dr. Carmen Canavier.

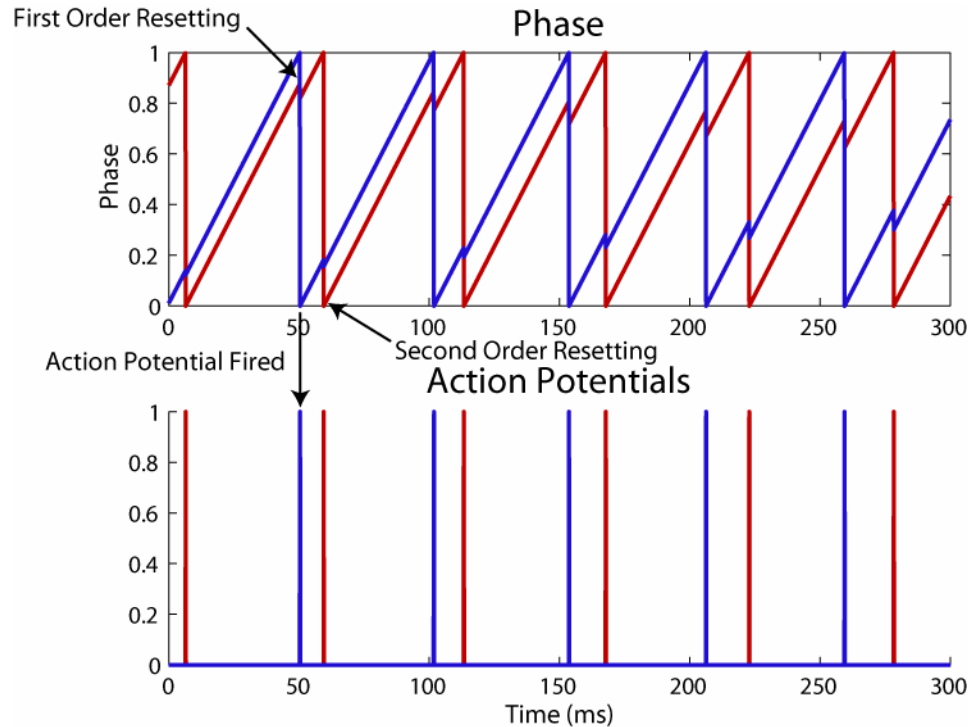


Figure 11. Example traces from the phase model simulator. Each neuron is a phase counter, which counts from the reset phase to one. When the counter reaches one, the phase is reset to the reset phase, and an action potential is fired. Firing an action potential immediately causes first-order phase resetting in the other neuron and sets the reset phase of that neuron to the phase indicated by second-order phase resetting. Second-order resetting is often small or zero, so it is difficult to visualize in this figure. Phase response is determined by the PRC curve fits described above.

3.1.5 Data Analysis

Data analysis for the experimental coupling results and the PRC simulations was performed using the same techniques. The first step of this process was to create raster plots of the phase differences between the neurons. This was done by measuring the spike time difference between a spike in the model neuron and a spike in the live neuron. This

time difference was normalized by the current firing period of the live neuron, as shown in Figure 12. This results in a phase difference from 0 to 1 with 0 and 1 being in-phase solutions, and a phase difference of .5 being anti-phase.

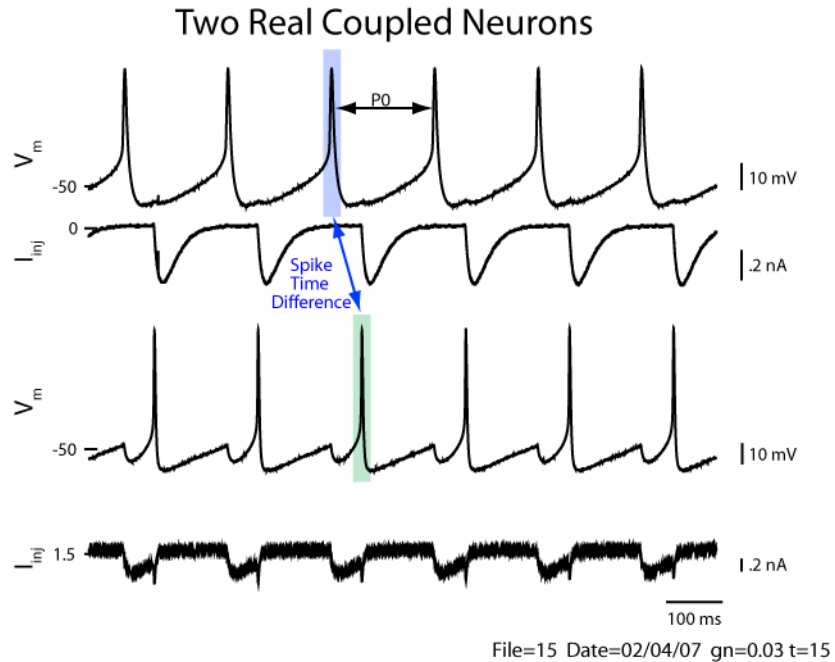


Figure 12. Example of how phase difference is calculated for coupled neurons. The spike time difference is calculated as the time from an action potential in the reference neuron (blue) to next action potential in the opposite neuron (green). This period difference is then normalized by dividing by the period of the reference neuron, P_0 .

For each set of coupling experiments, experimental and PRC simulations, we made raster plots of the phase differences as a function of time, as shown in Figure 13. Histograms were generated from the phase difference raster plots, also shown in Figure 13. These histograms show the phase difference on the y-axis to match the raster plots.

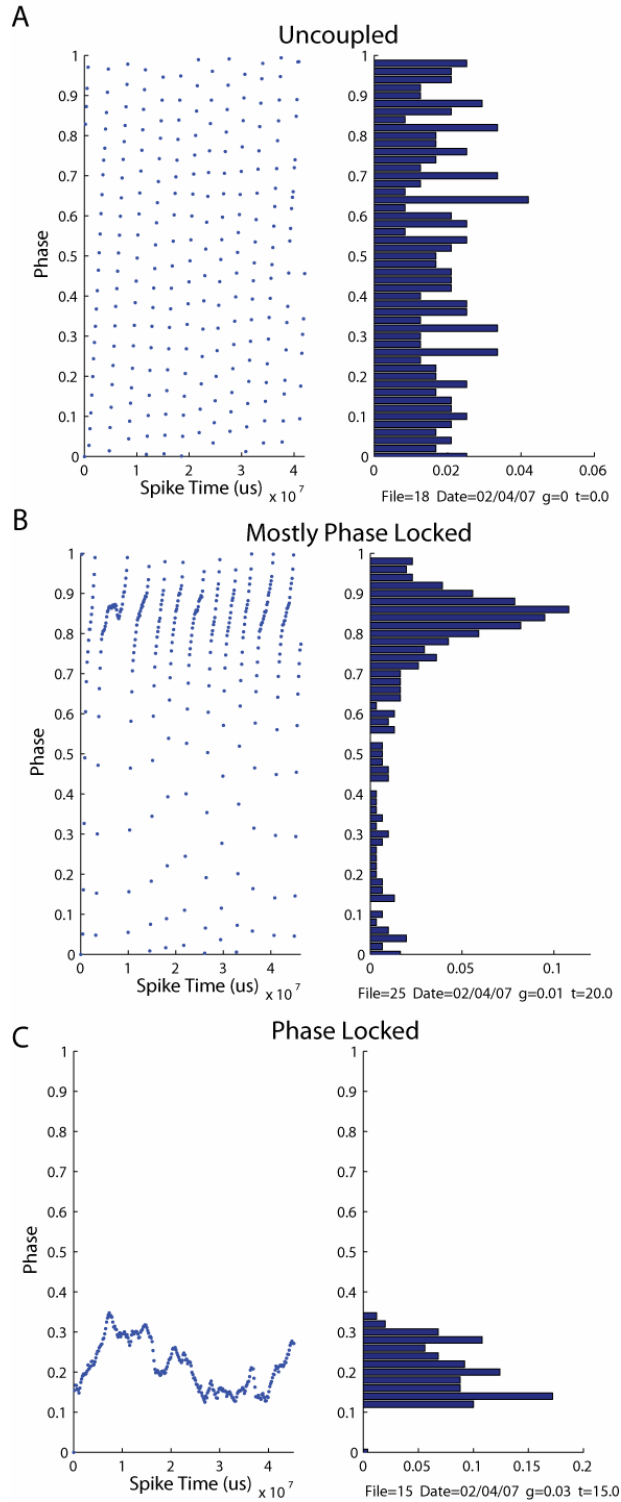


Figure 13. Phase difference raster plots and histograms for different degrees of phase locking. (A) Two uncoupled neurons, the histogram shows no dominant phase differences. (B) Two neurons that are mostly phase locked with the occasional phase walk through. The histogram shows one large peaks at phase difference of 0.8. (C) Phase locked neurons with no phase slipping. The histogram shows a phase difference of 0.2. Note: The phase locking in B and C is the same; the leading neuron in B is the live neuron, whereas in C, the leading neuron is the model neuron.

Next, the data from the histograms was rotated so that the phase difference is located along the x-axis, as shown in Figure 14A. Figure 14A shows multiple histograms in the same plot, as a way to compare phase-locking results for multiple synaptic time constants. This information is easier to visualize in Figure 14B, which contains pseudocolor plots of the histograms. In these plots, each histogram is represented as a horizontal row of colored squares, with the phase difference across the x-axis. The color of each square corresponds to the amplitude of the histogram. τ is displayed on the y-axis. This representation makes it is easier to compare the phase locking results across τ 's and between experiments and simulations. For a given τ , each row in the pseudocolor plot was normalized to the maximum histogram value to highlight the dominant phases for each synaptic time constant. For example, in this plot for a time constant of 3 ms, there are two major peaks, which can also be seen in the histogram in Figure 14A. As τ is increased, there is only one peak that continues to shift towards the in-phase solution of 1, until, at a τ of 7 ms, there is clear bistability between a phase difference of 0.75 and the almost in-phase solution, 0. In the transition from $\tau = 7$ ms to $\tau = 8$ ms, the synapses were turned off when they were turned back on to obtain the phase locking results, the neuron jumped to the in-phase solution for τ of 8 ms, which appeared to be extremely stable.

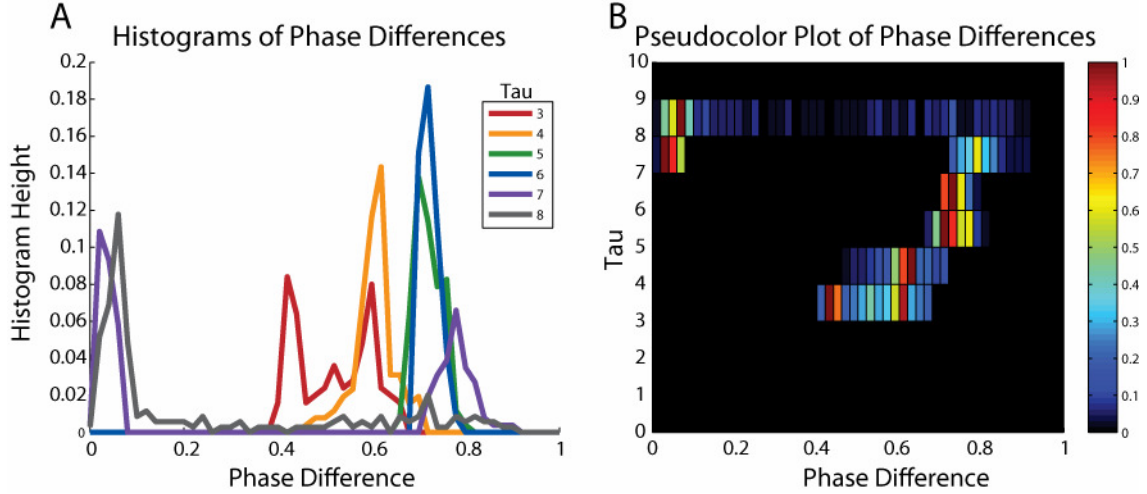


Figure 14. Example histogram and pseudocolor plots for multiple τ 's. (A) Phase difference histograms for multiple synaptic time constants plotted on the same graph. Instead of a normal bargraph histogram representation, a line connecting the amplitudes of the bars is plotted to allow more data to be displayed on one graph. (B) The histograms from A plotted as a pseudocolor plot. For each synaptic time constant, the histogram is normalized from zero to one to make the peaks of the histogram more obvious. Histogram amplitude is plotted as color, with the synaptic time constant, τ , along the y-axis, and the phase difference on the x-axis.

3.2 Results

The first goal of Aim 2 was to demonstrate that our inhibitory hybrid networks reproduced the transition from anti-phase to in-phase synchrony as the synaptic time constant is increased. Once this was verified, we used inhibitory coupling experiments to examine how the transition occurs and if it can be predicted from PRC data using either a phase model simulator or analytic solutions to existence and stability criteria.

3.2.1 Predicted and Observed Modes of Synchrony

The first goal of this research was to verify that our system would lock as predicted by the computational and theoretical literature, meaning it locks with anti-phase synchrony for fast synaptic time constants and in-phase synchrony for slow time constants. In addition, the hybrid network should display bistability between the two extremes of synaptic coupling. As described in the methods section, we turned the

synapses between our coupled neurons on and off to explore phase locking and bistability. We were able to qualitatively show both anti-phase and in phase-synchrony, as well as a range of bistability. Figure 15 A-D includes raster plots for increasing values of synaptic time constant, and the resulting histograms. The histogram data shows that for a synaptic time constant of 2.5 ms, the predominant phase locking is at a phase of .5. The phase locking for this time constant is less stable than the others, because the strength of the synapse is extremely weak. For time constants of 5 ms and 7.5 ms, the histograms and raster plots show bistability between a phase of .5 and a phase difference of 0/1. Finally, for a time constant of 10 ms, the in-phase solution is the only stable state for this experiment.

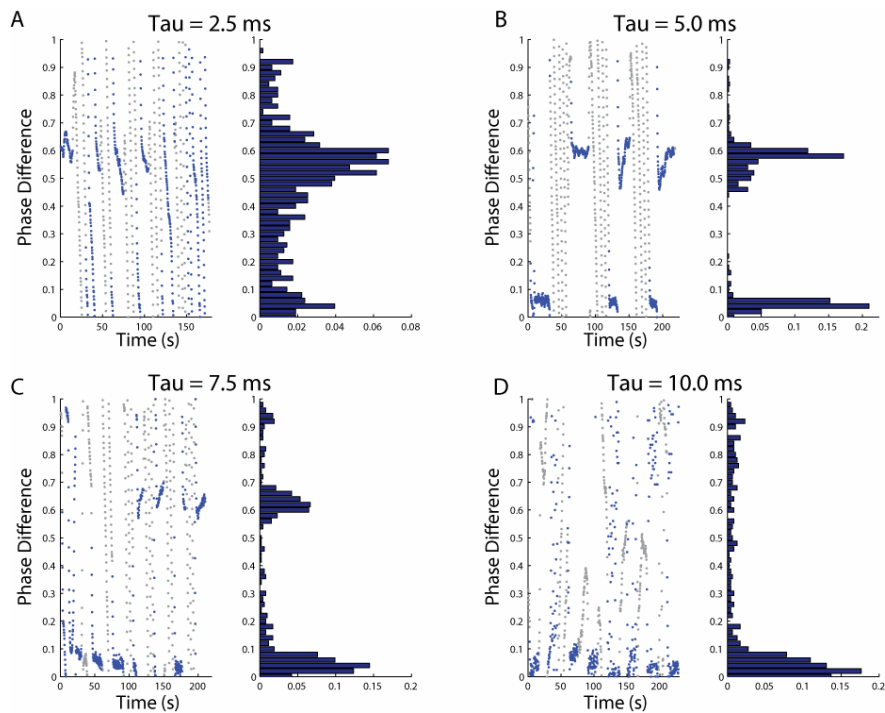


Figure 15. Qualitative bistability results. Raster plots and phase difference histograms for pulsed coupling experiments for different synaptic time constants. Synaptic coupling was pulsed on and off throughout each trial to locate all stable solutions. Coupling state is indicated by color of the dot; for magenta and cyan dots, coupling is off, for red and blue dots, coupling is on. (A) Synaptic time constant of $\tau = 2.5$ ms shows phase locking at approximately 0.5/ -0.5. (B) τ of 5.0 ms shows bistable phase locking at both 0.5/-0.5 and 0/1. (C) τ of 7.5 ms shows bistable phase locking at approximately -4/6 and 0/1. (D) τ of 10 ms shows phase locking at 0/1 (E) Plot of histograms from A-D with bars replaced by lines. This plot shows the transition from anti-phase to in-phase as the synaptic time constant is increased.

3.2.2 Transitions from Anti-Phase to In-Phase Synchrony

The results of the qualitative experiments described above led us to investigate how this transition from anti-phase to in-phase synchrony occurs. This was done by leaving the synapses on and incrementing the synaptic time constant in small steps. Figure 16 shows pseudocolor plots from three examples of this type of experiment. Experiments were started with small synaptic time constants that resulted in near anti-phase synchrony in each case. As the time constant was increased in small steps (τ increased approximately 1 ms every 1-3 minutes), the phase of locking increased or decreased monotonically towards the in-phase solution. At large enough time constants, phase locking jumped to the in-phase solution. In these experiments, for the low time constants displayed, the synapses were always on, so that unless spontaneous mode switching occurred, other stable modes were not detected. The gradual transition observed in these experiments is contrary to the abrupt mode switching that is predicted by computational and theoretical literature, but we show it for $n = 3$. The plots also display some data for higher time constants to verify that the in-phase solution continues to be stable. The synapses were turned off in between the coupling trials for these higher synaptic time constants.

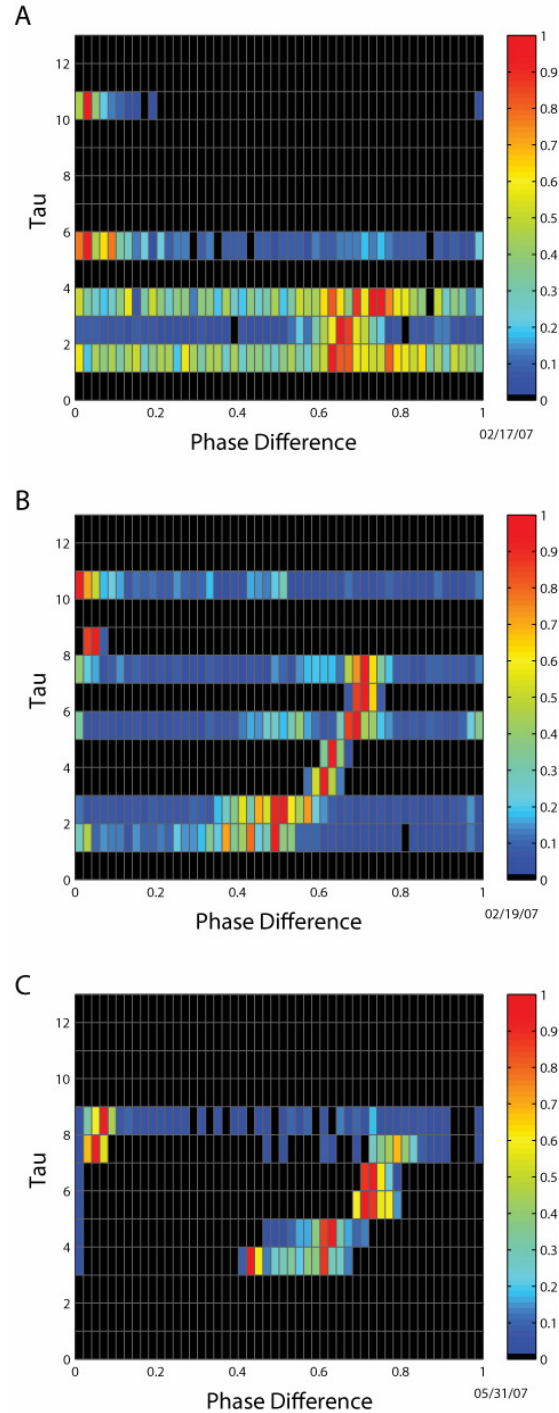


Figure 16. Pseudocolor plots of histograms including multiple τ 's from experimental coupling experiments for three separate neurons. Histograms with incremented synaptic time constants show a gradual transition from anti-phase to in-phase locking as a function of synaptic time constant. The solution eventually jumps to the in-phase solution, which appears to be more stable for higher synaptic time constants. (A) Synapses were on from $\tau = 2$ -4 ms; all other data were from separate trials. (B) Synapses remained on for all but the 8 ms to 11 ms time constant change. (C) Synapses were turned on for the lowest displayed synaptic time constant, τ , and increased every 1-3 minutes. Synapses were turned off between the $\tau = 7$ ms and $\tau = 8$ ms trials. For 3 ms – 7 ms, the synapses remained on as the time constant was slowly increased.

3.2.3 Synchrony Predicted by PRCs

PRCs were measured for each neuron used in the coupling experiments described above. These PRCs were used to predict the type of synchrony that the network would exhibit for a given synaptic time constant. Two different methods were used to predict synchronous solutions. First, PRCs were used to create phase models that were simulated and the resulting phase-locked solutions were observed. Then, the analytical criteria proposed by Dror et al. (1999) and Oprisan et al. (2004) were used to identify stable phase-locked solutions (Dror et al. 1999; Oprisan et al. 2004).

Phase Model Simulations

Phase models made from the PRCs measured in the above experiments were also used to predict the type of phase locking that would be exhibited as the synaptic time constant was increased. Figure 17 shows results from these simulations along with the experimental results and analytical predictions. The simulation results seem to show the same qualitative trends that experimental coupling produced, with intermediate areas of phase locking between the anti-phase and in-phase solution. However, the predicted results do not match the experimental coupling results well.

Analytical Solutions

Code provided by Dr. Carmen Canavier was used to analytically obtain the stable phase-locked states based on smoothing spline curve fits of the PRCs. This code uses the existence and stability criteria based on first-order and second-order phase resetting to solve for phase locked states that result from coupling the neuron PRC to the matched Wang and Buzsaki model PRC.

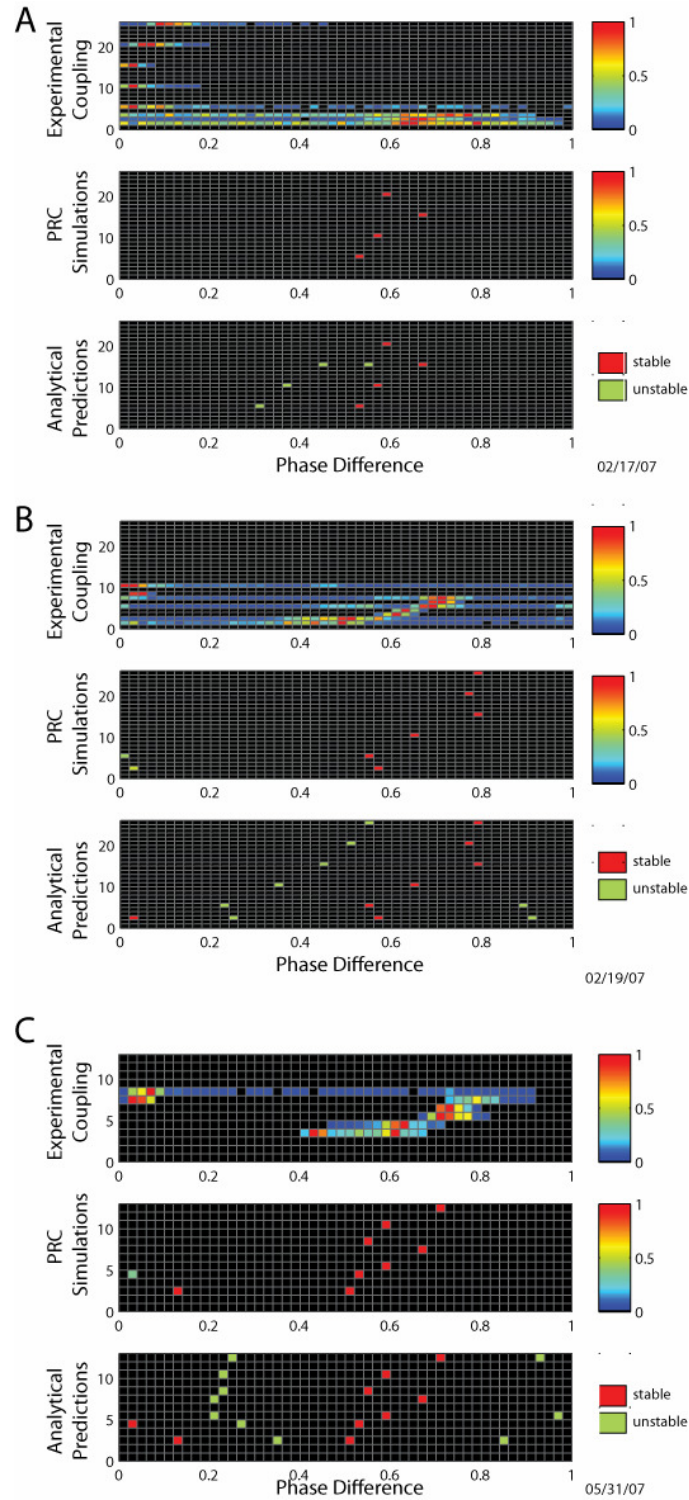


Figure 17. Pseudocolor plots of histogram results for experimental coupling, observed phase locking from PRC phase model simulations, and analytical PRC solutions for three separate experiments. (A)-(C) Experimental coupling shows a gradual transition from anti-phase to in-phase as the synaptic time constant, y-axis, is increased. Similar trends are seen for the stable solutions to the analytical predictions, and the PRC phase model simulations. For experimental coupling results, τ 's where there is no data indicate places where the synapses were turned off.

Figure 17 plots these results along with the histograms for phase-locking from the experimental coupling and the phase model simulator results. For these results, all phase-locked states are shown; stable states are plotted in red and unstable states are green.

3.3 Discussion

PRC theory and phase models are commonly used to computationally investigate network behavior. These simplifications are often used to develop analytical solutions that predict network behavior and increase computation speeds for network simulations. Though these simplifications are commonly used, they have not been fully investigated in live neurons. Previous experimental research in this area has either been done in bursting neurons, whose results do not directly scale to the computational research on tonically firing networks, or been in noisy cortical neurons that make it difficult to determine phase relationships and obtain phase locking (Elson et al. 2002; Merriam et al. 2005; Netoff et al. 2005b). These previous studies have only demonstrated in-phase and anti-phase synchrony as the time constant is increased, with bistability for the intermediate range of synaptic time constants. Besides the research described here, there has been only one other attempt at predicting phase relationships through phase models. Netoff et al. (2005) use spike time response curves to predict anti-phase synchrony for fast time constants and in-phase synchrony for slow synaptic time constants (Netoff et al. 2005b). They predominantly show anti-phase solutions for all but one of their inhibitory networks. Their results are obtained with a slowly changing background current designed to hold the neuron at a constant firing rate. This background current may alter phase-locking results, because coupled neurons do not fire at their intrinsic period, but a slightly different network period. Forcing this network period may affect phase-locking results.

The research presented here has been done in tonically firing neurons with an extremely constant firing rate. As such, we were able to demonstrate and measure phase locking with significantly greater precision than has been previously done. As predicted by current theoretical research, we show anti-phase locking for fast synaptic time constants and in-phase solutions for slow time constants (Van Vreeswijk et al. 1994). We also show regions of bistability between these two extremes. We were further able to investigate how this transition from anti-phase synchrony to in-phase synchrony occurs. This transition occurs gradually at first. When the phase difference becomes close to the in-phase solution, the network eventually jumps to the in-phase state, with some bistability.

In addition to allowing us to obtain accurate phase-locking information and examine the transition from anti-phase to in-phase, the constant firing rate also enabled us to measure PRCs that only contained small amounts of experimental noise. These PRCs were used to predict the types of network behavior observed in the coupled networks. Predictions were done using two different methods. Stable states were obtained analytically using the existence and stability criteria of Dror et al. (1999) and Oprisan et al. (2004) (Dror et al. 1999; Oprisan et al. 2004), and by simulations of phase models based on experimentally measured PRCs. Both sets of predictions qualitatively showed the same gradual anti-phase to in-phase transition observed in experimental coupling, as synaptic time constant was increased for all experiments ($n=3$). These solutions did not, however, fully reproduce the behavior of the experimental coupling results, because the in-phase solution was never obtained. We suspect this is due to noise in the PRC curve

fits, which have the most error at the edges (around zero and one), where the in-phase solutions would be obtained.

In this section, we were able to successfully predict qualitative trends in the phase-locking behavior of a hybrid inhibitory network using analytical solutions to the phase response curves. We confirm the anti-phase and in-phase solutions predicted in computational literature, but additionally show intermediate phase locking as the time constant is increased.

CHAPTER 4

DYNAMIC CLAMP STABILITY

The previous chapters demonstrated the utility of the dynamic clamp in electrophysiology experiments. It is an extremely powerful tool for integrating computational models with biological systems. Through real-time calculations, artificial conductances can be created and injected into biological neurons in a closed-loop feedback system. This technique capitalizes on both the complexity of real biological systems and the ability to manipulate computational models.

In performing the previously described dynamic clamp experiments, however, we discovered that the system displays transient instabilities under certain conditions. We verified that the instability was not caused by saturation of the electronics, as injected currents were not near the limits of the electronic equipment. The instability was also not caused by the numerics of the dynamic clamp system, which were well within the bounds described in Butera and McCarthy (Butera and McCarthy 2004). We also recreated our results using another dynamic clamp implementation (dSPACE DS1104, Paderborn, Germany) to verify that the instability was not an artifact of the MRCI system or the PC hardware. The instability was also reproduced in experiments using discontinuous current clamp instead of bridge balance mode. Such instabilities have also been reported by others through personal communication.

For Aim 3, we chose to study this instability, and the conditions that cause it. Through physical experiments and simulation, we show that dynamic clamp instability is directly related to the sampling delay of the dynamic clamp system and the maximum conductance of the current being simulated. The instability is exaggerated by

measurement errors caused by series electrode resistance compensation and stray capacitance in the electrode and electronics. We found that the maximum height of a step change of conductance that maintains a stable system increases dramatically when the delay in the dynamic clamp system is small and the series electrode resistance and stray capacitance are well compensated.

4.1 Methods

Investigating the dynamic clamp instability was done in several steps. Physical experiments were performed on both live neurons and a physical model of a passive membrane using a standard electrophysiology rig. We then created a computational model of the electrophysiology rig and dynamic clamp system to simulate the instability.

4.1.1 Physical Experiments

Electrophysiology experiments were performed as described in Section 1.3.1 Electrophysiology Experiments, with the dynamic clamp setup described in Section 1.3.2 Dynamic Clamp Technique. The MRCI Real-Time Linux based dynamic clamp was used to create a variety of conductances within both real cells and the Clamp-1U electrical circuit model cell (Molecular Devices Corporation, Sunnyvale, CA). The membrane voltage of a cell or membrane model was acquired and used by the MRCI system to generate ionic currents, which were fed back to the cell. Simulated currents were in the form of a time dependent conductance, $g(t)$, multiplied by the driving force: $I=g(t)(V_m-E_{syn})$.

4.1.2 Computational Model System

Two computational system models were used to replicate the experimental results obtained for both a spiking neuron and a passive membrane electrical model cell. The first was a simple computational model that included the effects of electrode resistance and capacitance. While this model produced some of the expected results, it did not fully reproduce the nature of the instabilities of our experimental data. As a result, we also use a more complete model that includes both the electrode effects and the effects of the amplifier, bridge balancing, and capacitance compensation circuitry. Two different computational neuron models were used to replicate both the spiking neuron experiments and the experiments with the Clamp-1U electrical circuit model of a passive membrane.

Neuron Models

Two separate neuron models were used. First, a tonically spiking neuron model based on the bursting pacemaker neuron in Butera et al. (Butera et al. 1999) was used to reproduce experimental results obtained for a tonically firing Aplysia neuron. This model is the first model described by Butera in that paper, with the $I_{\text{NaP-h}}$ current removed to eliminate bursting. The other computational model was a passive membrane, similar to the Clamp-1U artificial electrical model cell. Both models are shown in Figure 18. Two sets of parameters were used with the passive membrane model, one based on common invertebrate values and the other based on vertebrate values. For invertebrate simulations, the uncompensated electrode resistance, R_e , was 50 M Ω , with a membrane resistance, R_m , of 50 M Ω , and membrane capacitance, C_m , of 470 pF. Vertebrate simulations used an uncompensated R_e of 10 M Ω , an R_m of 500 M Ω , and C_m of 33 pF. These values are based on the values of electrical model cells used in the Clamp-1U and MCW-1U from

Molecular Devices (Sunnyvale, CA). Both simulations used an electrode capacitance, C_e , of 5 pF, unless otherwise noted. Simulations of this system were performed using Simulink (The MathWorks, Natick, MA).

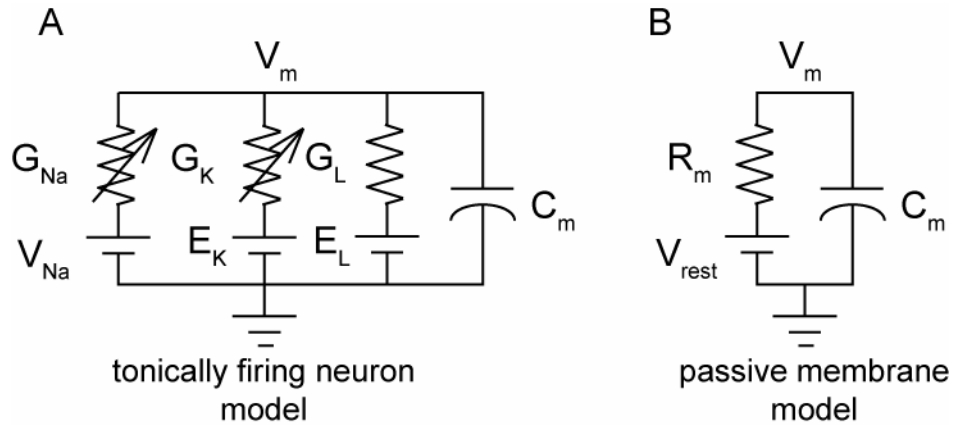


Figure 18. Computational neuron models. (A) Tonic firing neuron model used to reproduce experimental results obtained with a live tonically firing neuron. (B) Passive membrane computational model used to reproduce experimental results obtained with the Clamp-1U electrical model cell.

Electrode Model

The first system model we used to examine the behavior of the physical dynamic clamp system was quite simple. For this model, electrode effects were represented as a series resistance and a capacitor in parallel, to ground, as shown in Figure 19. R_e is caused by the properties of the electrode and the electro-chemical junctions between the neuron and microelectrode. The amount of R_e is compensated using electrical circuitry; however, compensation is imperfect, so there is some residual resistance. To model the effects of residual uncompensated resistance, the resistance value in our simulations was a percentage of the typical total electrode resistance. C_e is also caused by the electrical properties of the electrode. The glass of the microelectrode acts as an insulator between the two conducting liquids, potassium acetate in the electrode, and the saline bath solution outside. C_e also includes some of the stray capacitance present in the

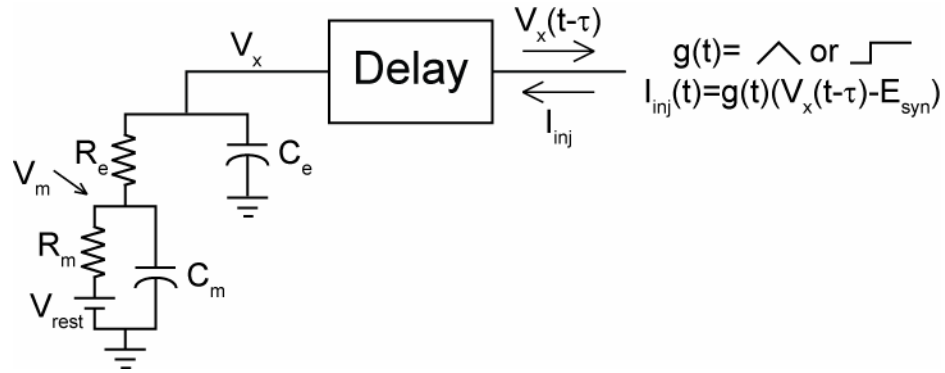


Figure 19. Electrode model with passive membrane. Simple model with electrode effects represented by a series resistance, R_e , and parallel capacitance, C_e . Dynamic clamp effects are represented by a delay in the membrane voltage, $V_x(t-\tau)$, used by the differential equations that would be simulated by the dynamic clamp during a physical experiment.

electrophysiological amplifier. For this model, the dynamic clamp latency, caused by data acquisition and computation time, was represented as a time delay in our simulations and stability analysis. Further analysis was done by replacing the delay with a zeroth-order sample and hold to model the effects of sampling more realistically. Quantization error was not modeled. Each computational neuron model was combined with the differential equations for the currents implemented in the dynamic clamp experiments, along with the electrode model, to create delay differential equations that model the entire experimental system. Equations 12-14 correspond to the passive membrane model system shown in Figure 19. This model includes a passive membrane (V_m , R_m , C_m), with electrode effects (R_e , C_e) creating the measured voltage V_x . The injected current, I_{inj} , is a constant conductance multiplied by the driving force calculated with a delayed measured voltage, V_x^d :

$$V'_m = \frac{\frac{V_x - V_m}{R_e} + \frac{V_{rest} - V_m}{R_m}}{C_m}, \quad (12)$$

$$V'_x = \frac{I_{inj} + \frac{V_x - V_m}{R_e}}{C_e}, \quad (13)$$

$$I_{inj} = g(t)(V'_x - E_{syn}). \quad (14)$$

Electrode and Amplifier Model

The second model we used to simulate the dynamic clamp instability was a more complete circuit model of the electrode and electrophysiology amplifier. This model, used by Park et al. (1983), includes equations to account for electrode resistance and capacitance, the bridge balance circuit, the capacitance compensation circuit, and other stray capacitance present in the amplifier (Park et al. 1983; Wilson and Park 1989). A diagram of this circuit, taken from Wilson and Park, is shown in Figure 20 (Wilson and Park 1989).

This diagram contains four major sections, the electrode and cell, the current injection circuit, the capacitance compensation circuit, and the bridge balance circuit. The far left section contains the circuit representation of the cell, Z_{cell} , and the electrode resistance and capacitance, $R_{electrode}$ and $C_{electrode}$. The voltage at V_{input} represents the uncompensated voltage that is a measure of the total voltage drop across the electrode and cell membrane. From this node, C_{shunt} represents the current flowing through the shunt capacitance on the amplifier, I_{cur} is the amount of command current, and I_{cc} is the current generated by the capacitance compensation circuitry.

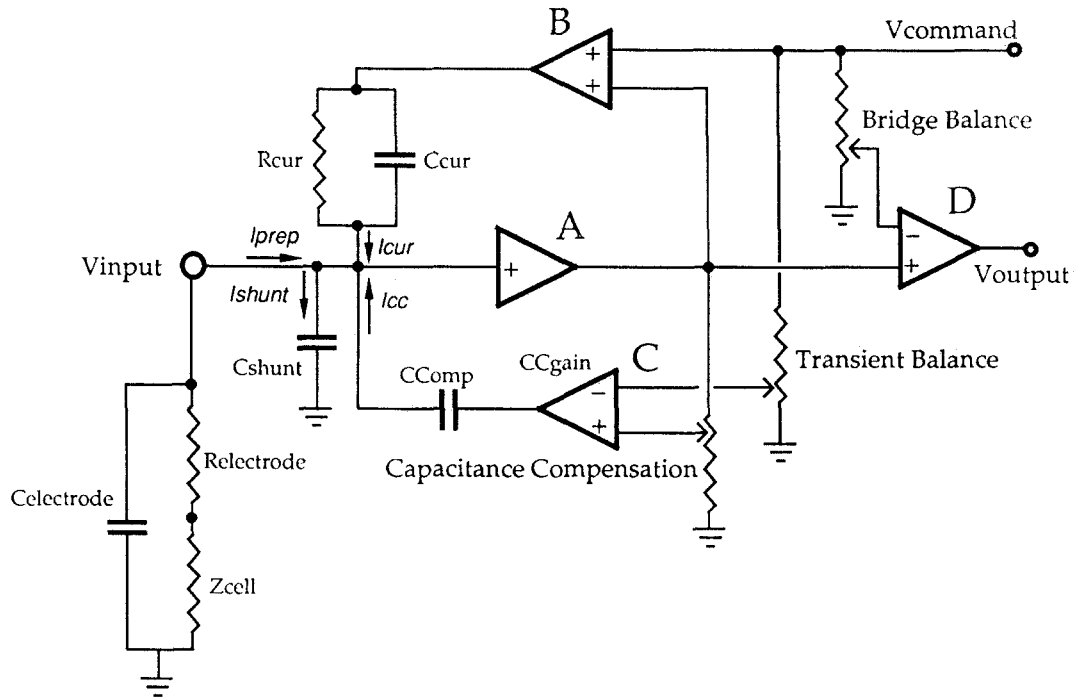


Figure 20. Electrode and amplifier model. Duplicated from Figure 1 of Wilson and Park (Wilson and Park 1989). It is important to note that this is a block diagram, not a circuit diagram; the elements correspond to the mathematical operations shown.

In the top portion of Figure 20, the command current, I_{cur} , is created from the command voltage, $V_{command}$. This voltage is converted into a current by passing it across R_{cur} , which is typically located within the electrophysiology headstage. To maintain a constant voltage drop across R_{cur} , independent of the voltage at V_{input} , V_{input} is added to $V_{command}$ at B. This circuit also contains C_{cur} , a shunt resistance in parallel with R_{cur} .

The capacitance compensation circuit is below the current injection circuit. This is designed to compensate for the current that is shunted by $C_{electrode}$, C_{shunt} , and C_{cur} . This circuit consists of two currents added together. First, the lower variable resistor, Capacitance Compensation, takes a portion of V_{input} , amplifies it by CC_{gain} , and injects it back into the V_{input} node through CC_{comp} . CC_{comp} corresponds to the knob on the

electrophysiology amplifier that is used to control capacitance compensation. This current is used to compensate for the C_{shunt} and $C_{electrode}$ currents. The other half of this circuit, labeled Transient Balance, is used to counteract the effect of C_{cur} by taking a portion of the command voltage amplifying it and passing it through CC_{omp} . C_{cur} is amplifier dependent and does not change from experiment to experiment. As a result, the Transient Balance control discussed here is typically not available to the electrophysiologist.

The final portion of the circuit is used to correct the measured voltage, V_{input} , by subtracting the voltage drop caused by the injected current flowing across the electrode resistance. This compensation is done by subtracting a portion of the command voltage, $V_{command}$, from the voltage at the input node. The amount of $V_{command}$ subtracted is set with the Bridge Balance. This setting corresponds to the Bridge Balance knob on most electrophysiology amplifiers.

This circuit, using a passive membrane model as the cell, is described by:

$$\frac{dV_m}{dt} = \frac{1}{C_m} \left(\frac{V_{in} - V_m}{R_m} - \frac{V_m - V_r}{R_m} \right), \quad (15)$$

$$\frac{dV_{in}}{dt} = \frac{1}{C_e} \left(I_{prep} - \frac{V_{in} - V_m}{R_e} \right), \quad (16)$$

$$I_{prep} = I_{curr} + I_{cc} - I_{shunt}, \quad (17)$$

$$I_{curr} = \frac{V_c}{R_{curr}} + C_{curr} \frac{dV_c}{dt}, \quad (18)$$

$$I_{shunt} = C_{shunt} \frac{dV_{in}}{dt}, \quad (19)$$

$$I_{cc} = C_{comp} CC_{gain} P_{cc} \frac{dV_{in}}{dt} - C_{comp} \frac{dV_{in}}{dt}. \quad (20)$$

For these equations and our simulations, I_{prep} is defined to be the opposite direction of that shown in Figure 20, and we assume the amount of Transient Balance is zero. We use V_m as the membrane voltage of the cell. V_{in} corresponds to V_{input} , V_c is $V_{command}$, P_{cc} is the amount of capacitance compensation, and V_r is the resting potential of the passive membrane.

Bridge balance compensation was implemented with:

$$V_x = V_{in} - P_{bb} V_c. \quad (21)$$

In this equation, V_x represents the compensated voltage, with the amount of compensation set by P_{bb} . For exact compensation, P_{bb} is equal to R_e/R_{curr} .

Table 2 shows the values used for each of the parameters described above. These values are similar to the values listed in Wilson and Park (Wilson and Park 1989).

Table 2. Parameter values for full electrode and amplifier model.

Parameter	Value
R_e	50 M Ω
C_e	3 pF
R_m	50 M Ω
C_m	125 pF
V_{rest}	-50 mV
R_{curr}	100 M Ω
C_{curr}	0 pF
C_{shunt}	1 pF
C_{comp}	1 pF
CC_{gain}	10

The dynamic clamp implementation is done using V_x as the membrane voltage used to solve the desired current injection equations. To reproduce the effects of the dynamic clamp sampling, the current equations that would be solved by the dynamic

clamp are calculated at the dynamic clamp sampling rate, while the rest of equations are simulated at a much faster rate. Simulations using this model were performed implementing a step one unit high times the maximal conductance g , multiplied by the driving force:

$$I_{inj} = u(t)g(V_x - E_{syn}). \quad (22)$$

This current was converted to the command voltage through a scale factor set by R_{curr} .

This computational model of the dynamic clamp has several advantages over the simpler model. First, we were able to test the full range of effects of bridge balance and capacitance compensation. For bridge balance, both under-compensation and over-compensation can be used; for capacitance compensation, the circuit model behavior matches the physical system in that it oscillates for over-compensation. This computational model demonstrated qualitative behavior similar to the physical experimental system.

4.1.3 Simulations and Stability Analysis

Simulations of both computational models were performed using Simulink (The Mathworks, Natick, MA). In addition, the stability of the delay-differential equations for the simple electrode model with a passive membrane model neuron was analyzed using the DDE-BIFTOOL package written for MATLAB (Engelborghs 2002). A current with a constant step of conductance multiplied by the driving force was used for stability analysis. The DDE-BIFTOOL was used to numerically locate the rightmost roots of the model system's characteristic equation, for a given set of parameter values. Our stability figures were produced by finding the maximum conductance where the system remained stable, i.e., contained only negative roots in the characteristic equation. We examined

how dynamic clamp latency, electrode resistance, and electrode capacitance affected the maximum conductance the stable system could have.

4.2 Results

The computational models were used to reproduce instability seen in the experimental system and to examine how the dynamic clamp latency, electrode compensation, and capacitance compensation affect the maximum amount of current that can be used with the dynamic clamp. The simple electrode model was first used to qualitatively reproduce the instability and then was studied using stability analysis. This model did not accurately reflect the effects of capacitance compensation seen in the physical system. As a result, the more complex model was used in simulations to determine the effects of these parameters. As a basic check, the characteristics were first compared to the results in the experimental system qualitatively, and then the simulations were used to quantitatively study how sensitive the instability is to the given parameters.

4.2.1 Physical Experiment and Simple Electrode Model Results

We first used physical experiments and the simple electrode model to examine the effect of the dynamic clamp sampling rate, the uncompensated electrode resistance, and the capacitance compensation on the stability of the dynamic clamp system. The physical system was used to show that these factors did affect how stable the dynamic clamp system was. The simple computational model was then used to qualitatively reproduce the same trends. Stability was measured as the maximum size of conductance step that could be used that maintained a stable system. This model showed that, as in the physical experiments, increasing the sampling rate and decreasing the amount of uncompensated electrode resistance maximized the amount of conductance that could be used while

maintaining a stable system. The results for capacitance compensation showed different effects. In the physical experiment, capacitance compensation improved the dynamic clamp system performance, whereas in simulation and stability analysis, it did not affect the performance. This disparity led us to change to the more complex system model.

Physical Experiments and Simulations

The simple electrode model was first used to qualitatively reproduce the instability. The experiments that initially identified a transient instability in the dynamic clamp system involved adding a slow potassium current, I_m , to a live spiking neuron. The current contained two state variables, a time-dependent activation variable and an instantaneous inactivation variable. As the maximum conductance of the current was increased, a transient ringing was observed at the end of the action potential, as shown in Figure 21. Experiments showed that this transient instability was affected by the rate of the dynamic clamp system, the electrode resistance compensation, the capacitance compensation and the maximum conductance of the current. The instability appeared as the conductance was increased.

To simplify this system, the voltage-dependent conductance was reduced to a voltage-independent up/down ramp multiplied by the driving force (Figure 22A). This type of current also resulted in instability as the maximal conductance was increased. The live neuron was then replaced with the Clamp-1U artificial model cell (Figure 22C). As with the real neuron, the system developed a transient instability as the conductance was increased.

Spiking Neuron with Transient Instability

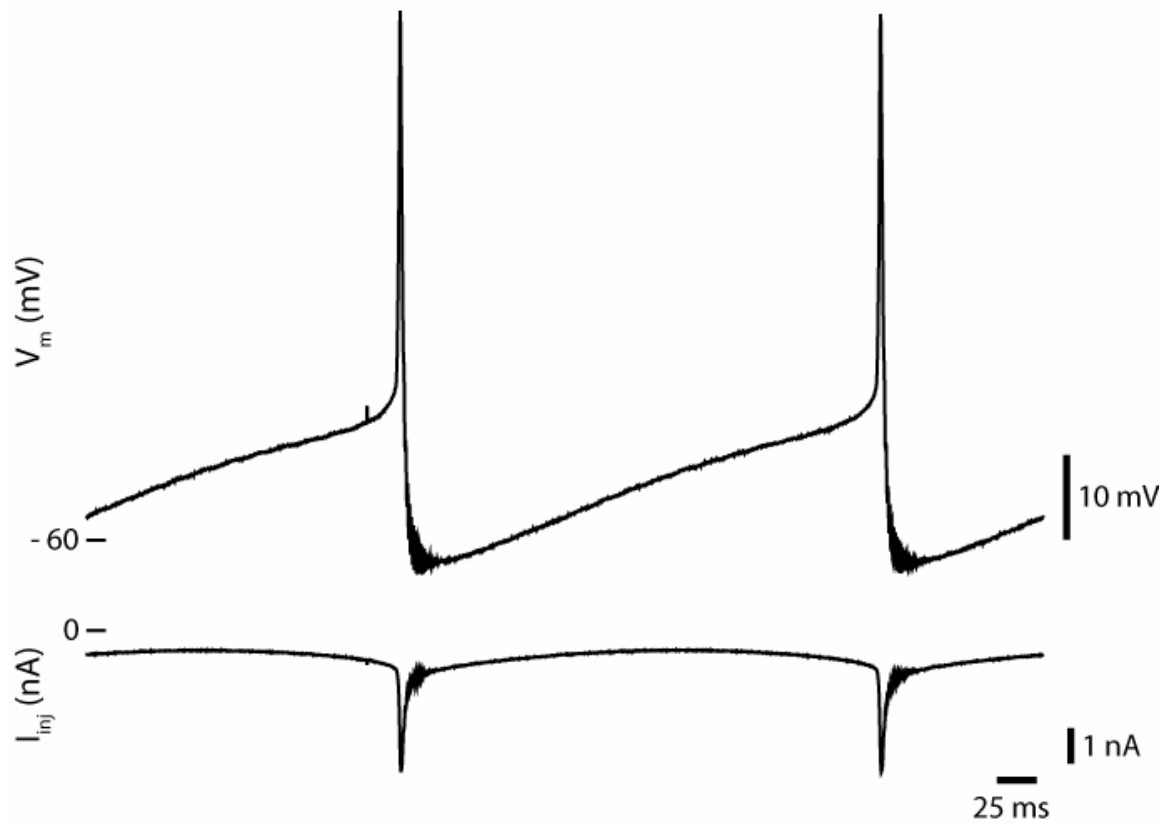


Figure 21. Instability demonstrated in a live neuron with a simulated slow potassium current, I_m .

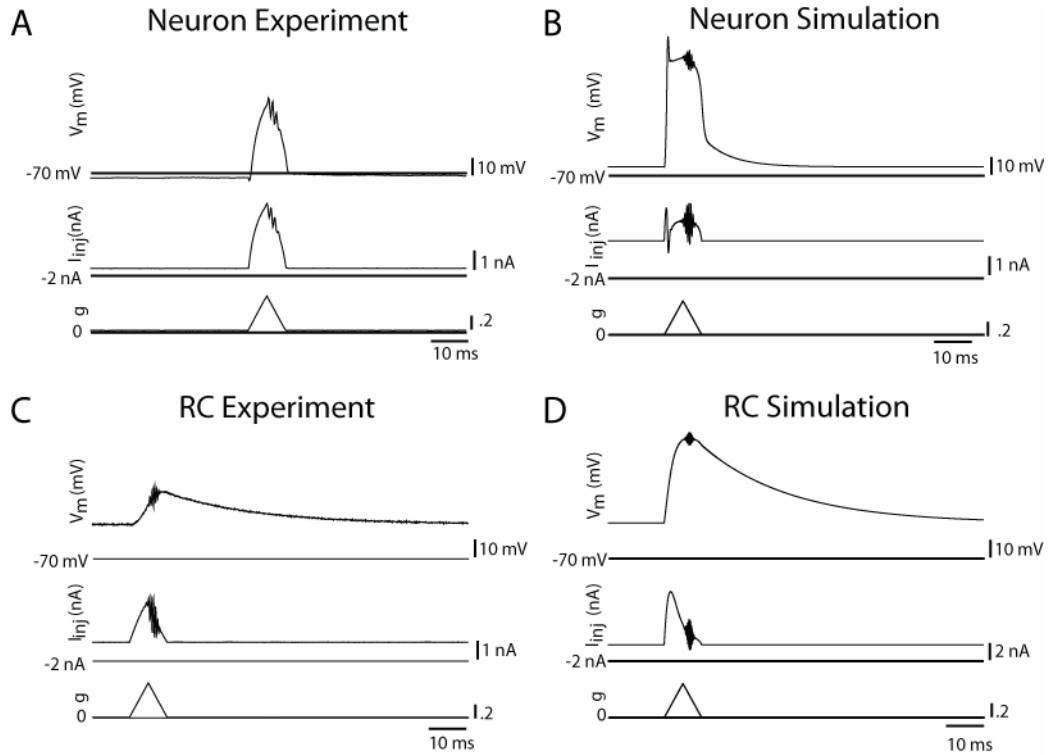


Figure 22. Experiments and simulations demonstrating dynamic clamp instability for spiking neurons and passive membrane models. (A) Live spiking neuron with ramp conductance. (B) Spiking neuron computational model simulation with ramp conductance. (C) Physical passive membrane circuit with ramp conductance. (D) Computational passive membrane simulation with ramp conductance.

We then used computational simulations to reproduce the instability seen in the physical experiments. Using the simple electrode model, we were able to reproduce the instabilities observed in the physical system. Figure 22B shows the transient instability in a spiking neuron model with an up/down ramp conductance current, using a residual uncompensated electrode resistance of $2 \text{ M}\Omega$ and an electrode capacitance of 1 pF . Figure 22D shows the transient instability in a passive membrane model ($R_m = 50 \text{ M}\Omega$, $C_m = 470 \text{ pF}$) with an up/down ramp conductance. The instability was also present when the slow potassium current, I_m , was used (not shown).

Stability Analysis

We next examined the stability of the delay-differential equations for the passive membrane model system using the DDE-BIFTOOL package written for MATLAB (Engelborghs 2002). Instead of a variable conductance, we used a constant step of conductance multiplied by the driving force. The DDE-BIFTOOL numerically located the rightmost roots of the model's characteristic equation, for a given set of parameter values. Our stability figures were produced by finding the maximum conductance where the system remained stable, i.e. contained only negative roots in the characteristic equation. We examined how dynamic clamp latency, electrode resistance, and electrode capacitance affected the maximum conductance the stable system could have. For this analysis, we focused on two sets of nominal RC parameters, referred to as invertebrate ($R_e = 50 \text{ M}\Omega$, $R_m = 50 \text{ M}\Omega$, $C_m = 470 \text{ pF}$, and $C_e = 5 \text{ pF}$), and vertebrate ($R_e = 10 \text{ M}\Omega$, $R_m = 500 \text{ M}\Omega$, $C_m = 33 \text{ pF}$, and $C_e = 5 \text{ pF}$). These are typical order-of-magnitude experimental values and correspond to the values used in the Clamp-1U and MCW-1U (Molecular Devices, Sunnyvale, CA), respectively.

Dynamic Clamp Sampling Rate

Figure 23A-B demonstrate the effect of dynamic clamp latency, or sampling rate, and electrode resistance on the maximum stable conductance for the simple electrode model using the invertebrate and vertebrate parameter sets. Each trace in the figures corresponds to a different amount of delay used in the model, while the x-axis shows increasing electrode resistance. For high sampling rates, a higher maximum stable conductance is attainable than for slower rates. The relationship has a sharp drop in the

maximum stable conductance for small changes in fast delays, and almost no change in the maximum stable conductance for longer delays.

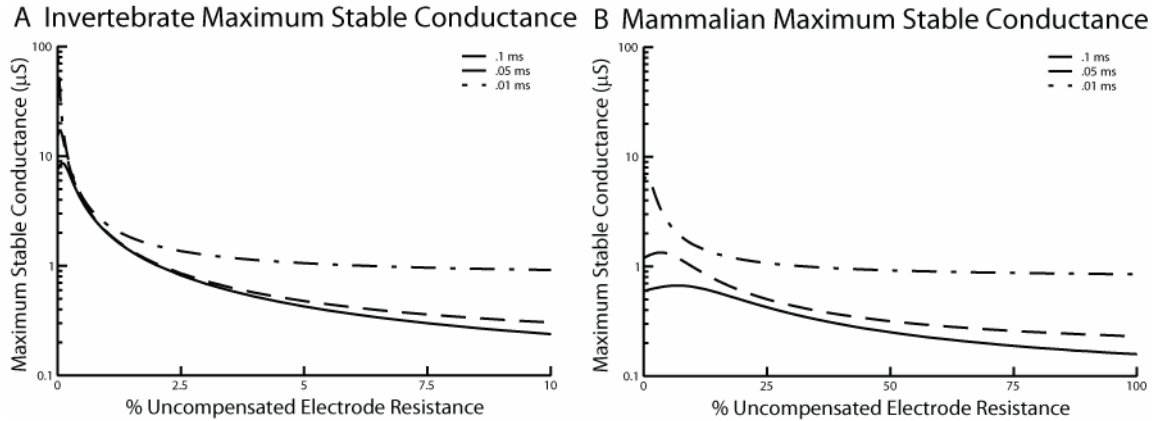


Figure 23. The maximum stable step conductance for invertebrate and vertebrate parameter sets as a function of sampling rate and electrode resistance. As the amount of uncompensated resistance increases, the maximum conductance step size decreases sharply. As the sampling rate increases, the maximum conductance step size increases rapidly. (A) Invertebrate parameter results. (B) Vertebrate parameter results.

Electrode Resistance Compensation

Figure 23 also shows the effect of electrode resistance compensation on the maximum stable conductance for both the invertebrate and vertebrate parameter sets. As the amount of uncompensated resistance is increased, the maximum stable conductance initially drops sharply. In addition, there is a finite maximum stable conductance for 100% electrode compensation, or zero electrode resistance. The axes in Figure 23 differ because of common electrophysiological practices. Electrode compensation is commonly performed in the sharp electrode invertebrate situation, where the electrode resistance and membrane impedance have similar magnitudes. Compensation is not commonly performed for patch clamping in vertebrate neurons because of the magnitude of the difference between the cellular input impedance and electrode resistance.

Electrode Capacitance Compensation

The results from stability analysis of the simple electrode model do not accurately reflect what was found in the physical experimental system. Figure 24 shows the stability analysis of the effect of electrode capacitance on the maximum stable conductance for the invertebrate parameter set. These results show that typical experimental values of electrode capacitance, 1 pF per millimeter of electrode immersion (Sherman-Gold 1993), do not significantly affect the maximum stable conductance of the system; however larger capacitances, not shown here, increase the maximum stable conductance. In contrast, we found experimentally that functionally decreasing the capacitance via compensation does have a noticeable effect on the maximum stable conductance. This result is accounted for in simulations of the more complex electrode and amplifier model.

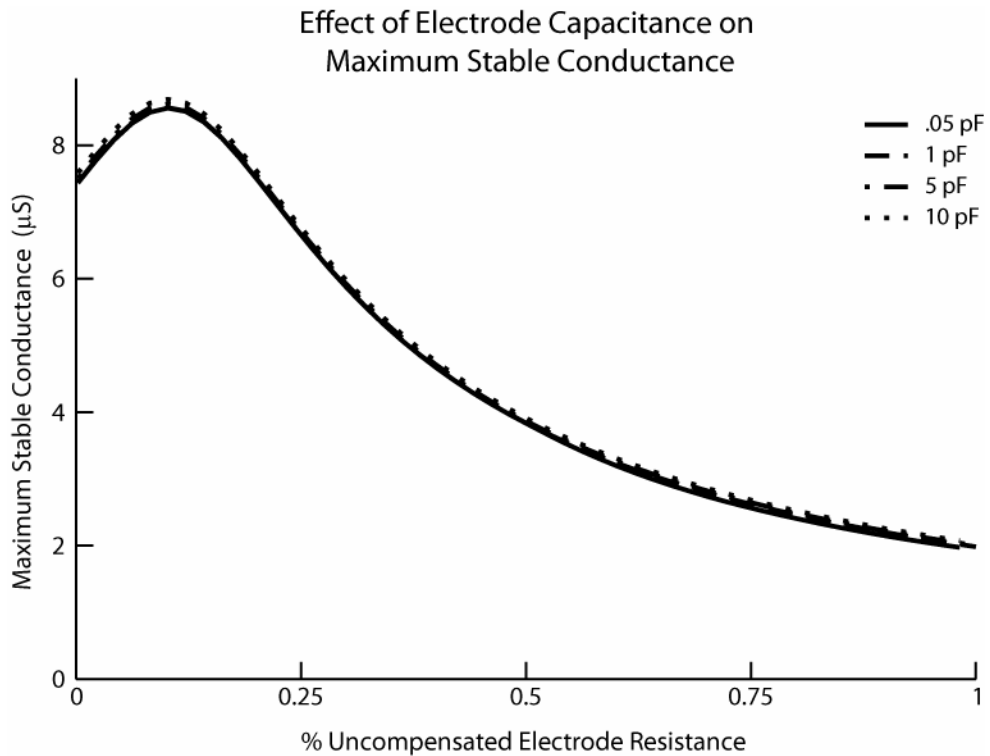


Figure 24. Stability analysis of the simple electrode model shows that, as the capacitance in the simple electrode model is varied, there is not a significant difference in the resulting maximum stable conductance.

Sample and Hold Effects

The simple electrode computational model used to perform the numerical stability analysis only accounts for delay in the dynamic clamp system; the measured voltage is simply delayed by the dynamic clamp latency. In the true system, however, the voltage is actually sampled at each time step and this value is held constant until the next computational time step. Although the simple delay model was able to reproduce the instability shown in the experimental system, we also performed simulations in Simulink to compare the effects of sample and hold to that of just a delay. Figure 25 compares the results of the simulations with sampling to the numerical stability analysis results. As can be seen from the figures, sampling and holding the membrane voltage further reduces the maximum stable conductance range for this experimental setup.

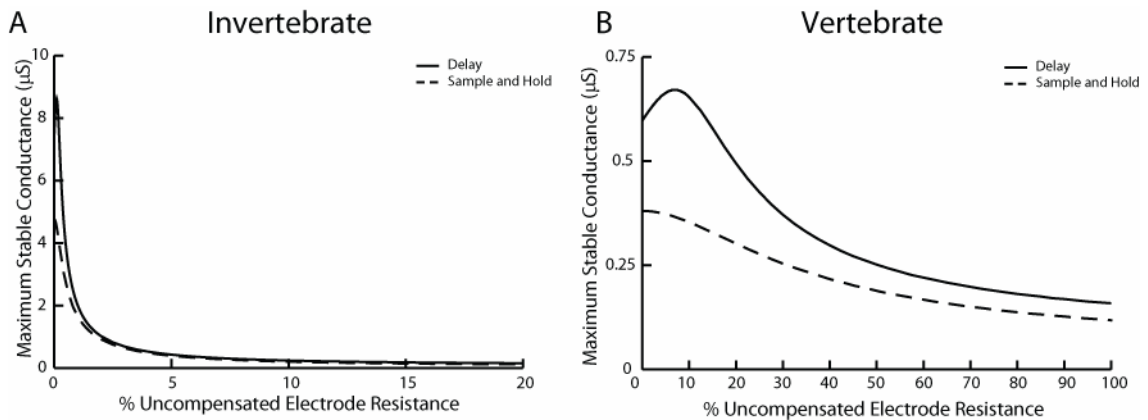


Figure 25. Sampling and holding the membrane voltage further reduces the maximum stable conductance step size for both parameter sets. (A) Invertebrate parameters. (B) Vertebrate parameters.

4.2.2 Electrode and Amplifier Model

The disparities between the physical experiments and the simple electrode model led us to use the more complicated electrode and amplifier model. This allowed us to reproduce the capacitance compensation results observed in the physical experiments. In

addition, it allowed us to more fully explore how over-compensation of the electrode resistance affects stability.

Model Step Response Characteristics

To verify that this model effectively simulated our physical system, we qualitatively compared the results to a current with a step of conductance for the cases when the bridge was balanced and un-balanced and the capacitance was not compensated and compensated. We found that the behavior matched very well.

Simulation Results

The electrode and amplifier computational model was then used to explore how the parameters affect stability in the dynamic clamp system. These results were found by determining the maximum possible step of conductance that maintains a stable system. This value was obtained by repeated Simulink simulations. To reproduce the dynamic clamp system's sampling effects, the equations describing the electrode and amplifier electronics were computed at one time step ($dt = 10^{-5}$ ms), while the equations that represented the amount of current being calculated by the dynamic clamp system were computed at the dynamic clamp sampling rate.

Electrode and Capacitance Compensation

Figure 26A-B show the results obtained when P_{bb} and P_{cc} , electrode resistance and capacitance compensation, were varied for a sampling rate of 10 kHz, using the parameters listed in Table 2. These parameters correspond to typical invertebrate intracellular values. For these values, full bridge balancing occurs when $P_{bb} = R_e/R_{curr}$, 0.5 for our parameters, and the capacitance is fully compensated at a value of $P_{cc}=0.5$. Figure

26 shows that the maximum stable conductance is a function of both P_{bb} and P_{cc} and contains a sharp peak when both electrode resistance and capacitance are well compensated, at $P_{bb} = 0.5$ and $P_{cc} = 0.495$. The capacitance compensation circuit is a positive feedback system that oscillates when the circuit is over compensated. As a result, the simulations oscillate for $P_{cc}=0.5$, so our closest results to full compensation are at $P_{cc}=0.495$.

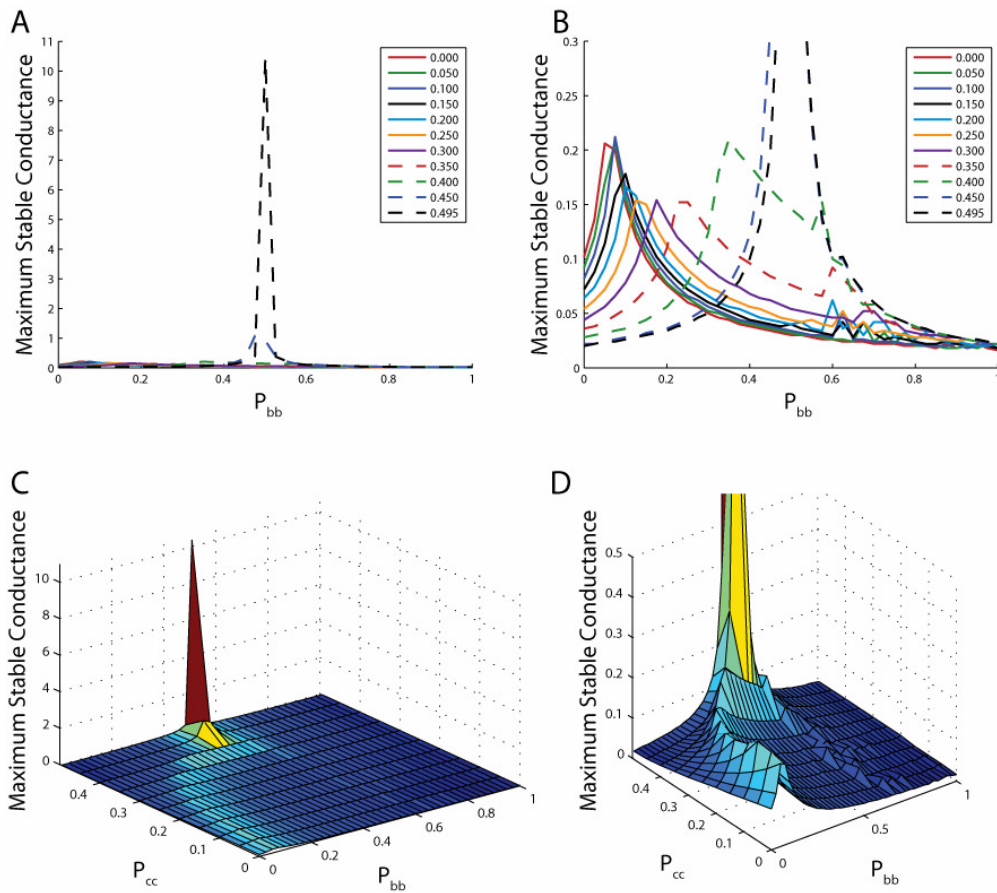


Figure 26. Maximum stable conductance as a function of P_{cc} and P_{bb} . (A) The maximum possible height of a step of conductance as a function of the amount of electrode resistance and capacitance compensation. The x-axis shows electrode resistance compensation; full compensation is at $P_{bb} = 0.5$. The traces correspond to different values of capacitance compensation; $P_{cc} = 0.5$ corresponds to fully capacitance compensated. (B) Figure A zoomed along the Y-axis. (C) 3-D plot of the effects of P_{cc} and P_{bb} on the maximum stable step conductance. Color corresponds to the logarithm of the maximum stable conductance. (D) Zoom of Figure C.

Dynamic Clamp Sampling Rate

Figure 27 A-B shows a comparison of the maximum stable conductance as a function of dynamic clamp sampling rate for sampling rates of 5 kHz and 10 kHz. The increased sampling rate drastically improves the peak value (Figure 27C); however, the cases without perfect compensation show mixed results. For significantly under compensated cases performance increases with sampling rate; however for moderately compensated results, performance decreases with sampling rate. Figure 27C shows the peak value of maximum stable conductance, located at $P_{cc} = .495$ and $P_{bb} = 0.5$ as a function of the sampling rate. This plot highlights how much improvement faster sampling rates provide for the compensated case.

Injection Shunt Capacitance

The current injection resistor, R_{cur} , has a stray capacitance, C_{cur} , in parallel with it. This is balanced by the P_{tb} control. The affect of C_{cur} is shown in Figure 28. Surprisingly, this stray capacitance appears to have a beneficial effect in these simulations. It is possible to obtain higher amplitude steps for larger values of C_{cur} . This is because C_{cur} is responsible for over-emphasizing the high frequency components of the injected current waveform, producing artificially sharp steps of current. This effect is noted by Wilson and Park (1989). They show that C_{cur} produces a boost to the initial transient of injected current, causing what appears to be an improvement in the response of the circuit, (Figure 2B (Wilson and Park 1989)). This apparent improvement becomes an overshoot in injected current as the effects of C_{cur} and other circuit capacitances are compensated.

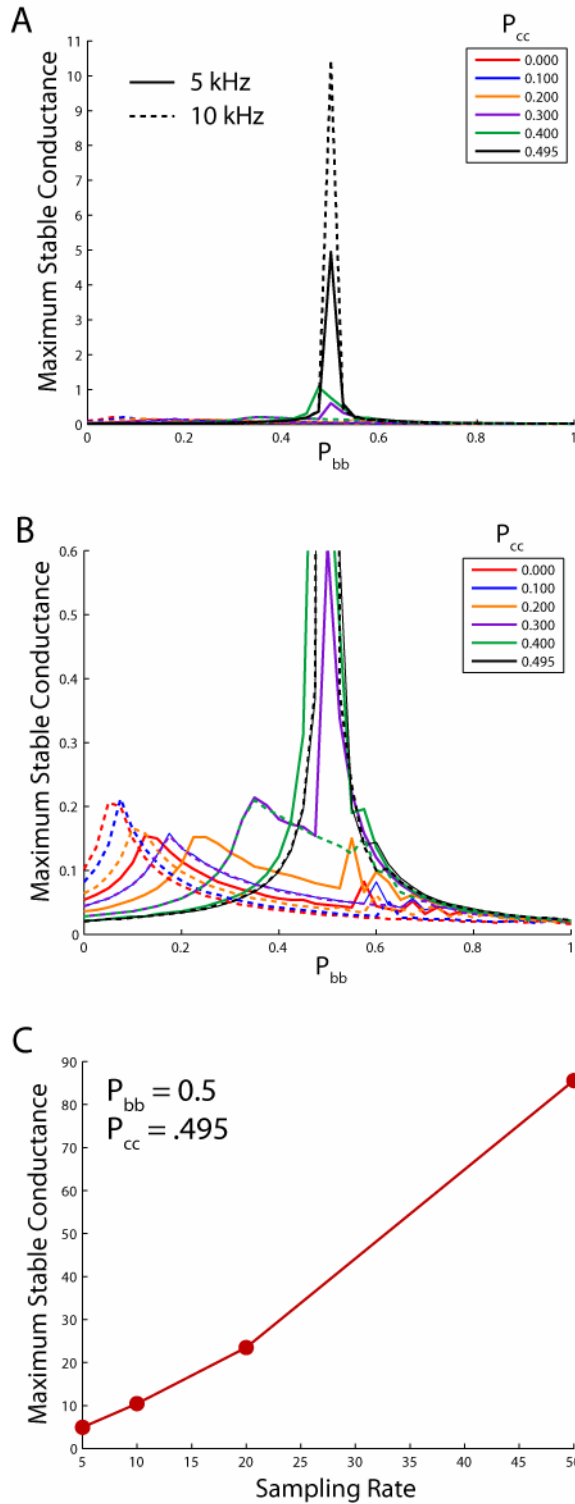


Figure 27. The effect of sampling rate on the maximum stable conductance. (A) The maximum stable conductance for a variety of P_{bb} and P_{cc} values, for a 5 kHz sampling rate and 10 kHz sampling rate. (B) A zoomed version of A. (C) Plot of the maximum stable conductance as a function of τ for the completely compensated case, $P_{bb} = 0.5$ and $P_{cc} = .495$. The maximum stable conductance increases dramatically with sampling rate for the compensated value.

The overshoot for compensated circuits is responsible for the lower maximum stable conductances observed for capacitance compensated circuits ($P_{cc}=.495$) that contain C_{cur} , as shown in Figure 28.

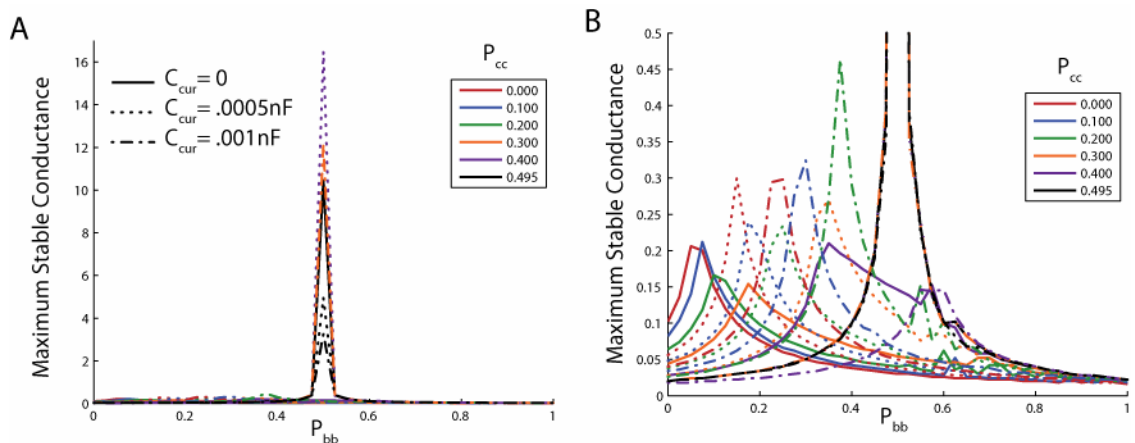


Figure 28. The effect of C_{cur} on the maximal stable conductance. Line style indicates C_{cur} value - solid lines: $C_{cur} = 0$ nF, dotted: $C_{cur} = .0005$ nF, dot-dash: $C_{cur} = .001$ nF. (A) Overall effect of C_{cur} . C_{cur} emphasizes the high frequency components of the injected step of current, causing under-balanced situations to behave well balanced, while causing overshoot for capacitance compensated circuits. (B) Figure A zoomed along the y-axis to show detail. C_{cur} shifts maximum stable conductance peaks to occur at higher P_{bb} and be slightly larger.

4.3 Discussion

The dynamic clamp technique has been used to greatly enhance our knowledge of neurons and networks of neurons. By adding or subtracting ionic currents through real-time model simulation, the dynamic clamp has shown how individual currents affect the activity of a cell and how pharmacological agents affect cell properties. The dynamic clamp is also used to generate synaptic coupling between neurons to study how individual neurons and synapses affect network behavior.

This widely used technique has some known limitations. The temporal dynamics of the simulated currents are limited by the speed of the dynamic clamping system. The accuracy of the calculations is limited by the numerical methods used, quantization error,

latency, and jitter present in the dynamic clamp system. Faster integration techniques, such as the exponential Euler method, are often used to perform computations faster, at the sacrifice of precision.

This chapter presented a final limitation resulting from a combination of these factors. The dynamic clamp system becomes unstable under certain situations. This phenomenon has been personally reported by numerous dynamic clamp users, using different dynamic clamp implementations. It is present in both vertebrate and invertebrate setups, under both bridge balance and discontinuous current clamp modes. We have verified that it is not a direct result of quantization error, saturation of the electrical equipment, or the type of dynamic clamp system used.

The primary cause of this system instability is the latency in the dynamic clamp system. This delay is caused by the time needed to sample the membrane voltage and perform the required calculations. Current dynamic clamp systems run at speeds from 2 kHz – 20 kHz, or latencies of .5 ms – .05 ms. The dynamic clamp running speed depends on both the complexity of the model being simulated and the dynamic clamp system. Investigators typically justify their choice of dynamic clamp rate in terms of the kinetics of the ion channel being simulated. This work shows that stability may impose more stringent rate requirements, especially when using higher value conductances.

The relationship between the delay and the maximum stable conductance suggests that more effort should be put into developing faster dynamic clamp systems. Not only would a faster system increase the possible temporal dynamics, it would also increase the allowable model complexity and the effective range of the system. Faster rates allow the currents to be simulated with higher conductances, or feedback gain.

Currently, there are a number of commonly used dynamic clamp systems. These implementations range from dedicated analog or digital hardware to personal computer-based systems. Dynamic clamp systems on dedicated hardware are extremely fast because they are only limited by the time it takes to perform the calculations for the computational model; however, they are less flexible and more expensive. Implementations based on personal computers are limited in absolute maximum speed by the operating system they run under. Previously, it was thought that this only affected the temporal dynamics of currents being simulated by the dynamic clamp; however this research proves it is also important for stability.

The second major cause of system instability results from the complications of measuring voltage and injecting current through the same electrode. In electrophysiology experiments using bridge balance techniques to compensate for electrode resistance, the membrane voltage measurement is affected by how well the compensation is performed. The general procedure for bridge compensation involves the experimentalist applying a step of current and using a knob (P_{bb}) to visually eliminate the voltage change caused by this step of current. Under-compensation or over-compensation causes error in the voltage measurement that is then used by the dynamic clamp. Compensation is usually only performed once or twice during an experiment, in spite of electrode properties changing throughout an experiment. The same types of effects also occur under discontinuous current clamp. In this case, measurement error comes from an insufficient settling time. For discontinuous current clamp systems, the sampling rate also limits the effective speed the dynamic clamp can be run at.

The experimental procedure for capacitance compensation is also a rough approximation. In this process, the experimentalist adjusts a different knob (P_{cc}) in an effort to minimize the capacitive transients at the edges of the injected current step. Unlike bridge balance compensation, it is not usually possible to even quantify the amount of compensation being used. The capacitance compensation circuit used is a positive feedback circuit that becomes unstable when over-compensated.

Results for the slightly under-compensated case, $P_{cc} = .495$, show a dramatic increase in the size of step conductance that is possible when the electrode resistance is fully compensated. The peaks of the maximum current step size is a function of both electrode and capacitance compensation, as shown in Figure 26. For the unbalanced case, there are small peaks in the maximum step of current that vary with both P_{cc} and P_{bb} . As the capacitance compensation is increased, the peaks occur for higher bridge balance compensation, and are larger in magnitude. These variations are small, however, when compared to the large increase in possible maximum step of conductance, when both quantities are completely compensated.

The capacitance present in the current injection circuit, C_{cur} , appears to provide an improvement in the dynamic clamp performance. This shunt current overemphasizes the initial transients of currents that result from step changes in conductances, creating sharp edges in the injected current. This capacitance is beneficial for step results, but may distort the shapes of other waveforms, for instance, the shape of an action potential or time and voltage varying current. As a result, manipulating C_{cur} is not a good method for improving dynamic clamp performance.

Standard methods for electrode resistance and capacitance compensation rely on the experimentalist's visual inspection and adjustment of the amount of compensation. This crude method of compensation is generally performed once at the beginning of the experiment. The development of active compensation that more accurately compensates and adapts to changing electrode resistance and capacitance throughout an experiment would significantly reduce the effects of electrode resistance and capacitance on the stability of dynamic clamping systems, and allow users to take full advantage of performance increases that result from using faster dynamic clamp sampling rates.

CHAPTER 5

CONCLUSIONS

The nervous system is made up of large networks of coupled neurons that are important for many different activities. The configurations of these networks produce different modes of behavior, including synchrony and phase-locking. In the brain alone, synchrony and phase-locking has been implicated as a mechanism for memory, cognition, sensory processing, motor planning, and execution. Many neurological diseases, including Parkinson's, schizophrenia, and epilepsy, are the result of abnormal synchronization. A clear understanding of the basic mechanisms that produce synchrony and phase locking will ultimately allow us to repair or replace functionality lost through illness and accident.

Studying neuron coupling and the resulting network behavior experimentally is difficult for a number of reasons. First, the amount of information available about a network is severely limited, even for small networks. When specific neuronal parameters are known, it is difficult to manipulate these parameters, and eliminate extraneous network input. As a result, there is a significant amount of computational research investigating how network parameters contribute to network behavior and more specifically synchrony and phase locking. These computational studies also have limitations. The amount of memory and computation time needed to simulate highly detailed biophysical models makes simulations of even small networks rather slow. As a result, several common assumptions are used to create much simpler neuron models, known as phase models, which can not only be used for computational simulations, but also allow for analytical analysis of possible network behavior.

The overall goal of our research is to use electrophysiological experiments to verify results and assumptions found in computational research related to coupling and synchrony in neuronal networks. For this project, we used the dynamic clamp technique to examine two specific assumptions. First, we verified that the weak coupling assumption, which is often used to simplify network simulations and provide a method for obtaining analytical results, is valid in live neurons for appropriately sized inputs. We next looked at the use of phase models to predict synchrony as a function of synaptic coupling time constant. Finally, we examined the dynamic clamp technique, which is often used in network studies to create networks of live neurons or hybrid networks by creating artificial neurons and synaptic coupling.

5.1 Weak Coupling

Chapter 2 described electrophysiology experiments to validate the weak coupling assumption. The weak coupling assumption is often made in simulations and analytical solutions to predict network behavior. It is based on the ideas that the neuronal oscillator is on a strongly attracting limit cycle and that stimuli are weak and do not perturb it far from this limit cycle. The assumption states that the phase response of a neuron is equal to the convolution of an IPRC (an intrinsic neuronal property) and the stimulus function. This convolution function makes it possible to separate the stimulus from the neuronal response. This is commonly used in computational analysis, allowing one to reduce a network model of phase oscillators to a system of variables representing phase differences. Although it is not commonly used in electrophysiology experiments, it would allow one to characterize a neuron's response to stimuli by measuring a single PRC,

instead of one for each stimulus. It would also simplify studying the case of multiple inputs per cycle.

Our research showed that the weak coupling assumption holds for invertebrate neurons from *Aplysia californica*. We have shown that small amplitude stimuli evoke PRCs that scale linearly with stimulus amplitude, but that strong amplitude PRCs do not. We have also shown that IPRCs deconvolved from PRCs can accurately predict the phase response of a neuron to other stimulus waveform shapes, for weak stimuli. When the IPRCs are convolved with a stimulus waveform, the resulting predicted PRC matches the experimentally measured PRCs for that stimulus shape. The amount of error between the predicted and actual PRC grows as the stimulus amplitude increases.

The observed region where IPRCs can predict the phase response of a neuron is within the normal range of synaptic input experienced by these neurons. This proves that weak coupling is not only a possible method of coupling, it is a likely mechanism for these animals. This information validates numerous computational studies based on this assumption, and opens the door to more complex biological experiments.

5.2 Coupling and Phase Response Curves

Chapter 3 explored how well phase models can predict the behavior of inhibitory hybrid networks. Again, this research was motivated by a significant amount of computational literature that had no accompanying experimental verification. We verified that fast synaptic coupling for our neurons resulted in anti-phase synchrony, while slow coupling led to in-phase synchrony. We showed that there is a region of bistability in between these two extremes. These experiments led us to investigating how the transition between anti-phase and in-phase synchrony occurs. We showed, through experimental

coupling, that the transition is gradual, instead of the abrupt mode switching predicted by the computational literature. We showed that the phase difference between the two neurons changes with synaptic time constant, until it is close to the in-phase solution, and then it jumps to this mode of synchrony, perhaps with bistability. This work also used experimental PRCs measured from the same cells to predict the type of synchrony that would occur for the networks of neurons. Predictions based on analytical solutions of the PRCs also showed the gradual transition from anti-phase to in-phase that was present in electrophysiological experiments, as did phase model predictions. However, neither set of PRC predictions identify the in-phase solutions seen in experimental coupling. We suspect this is due to noise in the curve fitting at the ends of the PRC data.

This research leaves several open questions that need investigation. First, our current research only tested the effect of synaptic time constant on synchrony in inhibitory networks. The effects of synaptic coupling strength could also be studied. In addition, future network studies containing two live neurons coupled through artificial synapses would also be beneficial. Finally, the mechanism behind the gradual transition from anti-phase to in-phase synchrony is an intriguing one that needs further investigation. This is not predicted by current computational literature in coupling and synchrony.

5.3 Dynamic Clamp Stability

Chapter 4 explored instability present in the dynamic clamp system. This technique is often used to combine real-time computational simulations with electrophysiology experiments. Our research was motivated by the first two specific aims described in Chapters 2 and 3. In performing those experiments, we often found that the

dynamic clamp system would become unstable as the maximal conductance of the simulated ion channel was increased. This same problem had also been reported by others through personal communication. As a result, we examined what factors affect the instability, in an effort to improve dynamic clamp performance.

Experimentally, we determined that the maximal conductance, dynamic clamp sampling rate, electrode resistance, and electrode and amplifier capacitance all affected when the instability appeared. After obtaining a qualitative understanding of how these parameters affected stability, we developed two models of the dynamic clamp system to reproduce the instability and quantitatively examine how each parameter contributed to it.

The first model was designed to simulate microelectrode effects and the dynamic clamp sampling delay. It was a simple model consisting of a resistor and capacitor in parallel to model the effects of injecting current through an electrode. The dynamic clamp was implemented as a pure delay equal to the sampling rate of the dynamic clamp system. This simple model qualitatively reproduced the instability observed experimentally, and the effect of uncompensated electrode resistance showed the same trends as the experimental observation; however, this model did not accurately reflect how capacitance compensation affected the instability in the physical setup.

As a result, a more complex model simulating the electrode resistance and capacitance, as well as the amplifier circuitry, including current injection, capacitance compensation, and bridge balancing was used. This model accurately captured how these parameters affected stability in the experimental setup. Specifically, when the electrode is perfectly bridge balanced, and the capacitance is adequately compensated, there is a dramatic increase in the amount of maximal conductance that can be used compared to

other conditions. In addition, increasing the sampling rate also dramatically increases the acceptable amount of maximal conductance for the well-compensated case.

Future work in this area includes implementing improvements to the dynamic clamp techniques to increase its stability. Specifically, better electrode resistance and capacitance compensation techniques would dramatically increase the usable range of the dynamic clamp. Existing compensation techniques are crude and static, while it is known that the electrode properties change throughout an experiment. Active, automatic compensation would increase the usable range considerably. Once accurate and consistent bridge balancing is possible, increases in dynamic clamp sampling rates would further increase the dynamic clamp range.

5.4 Conclusions

Computational modeling provides a powerful tool for examining the mechanisms involved in neuronal and network behavior. Models provide a way to create and examine simple systems where all of the parameters are visible and able to be manipulated. It is important, however, that results and assumptions used in computational modeling be validated within biological systems. The research presented here validated a few common assumptions and computational results and investigated a popular tool for combining electrophysiology experiments with computational simulations.

APPENDIX A

WANG AND BUZSAKI MODEL NEURON

The coupling experiments in Chapter 3 used a hybrid network of one live neuron and one Wang and Buzsaki model neuron (Wang and Buzsaki 1996). The Wang and Buzsaki model was chosen because its PRC is similar to the tonically firing neurons from the abdominal ganglia of *Aplysia californica*. Both types of neurons exhibit Type I phase resetting, with similar PRCs. The firing rate of the Wang and Buzsaki model can be controlled through modification of the I_{app} current so that it fires at a rate similar to the biological neuron. The equations used to implement this model are

$$\frac{dv}{dt} = \frac{1}{C_m} (-I_{Na} - I_K - I_L - I_{syn} + I_{app}), \quad (23)$$

$$I_{Na} = g_{Na} m_{\infty}^3 h (V - E_{Na}), \quad (24)$$

$$m_{\infty} = \frac{\alpha_m}{\alpha_m - \beta_m}, \quad (25)$$

$$\alpha_m(V) = \frac{-0.1(V + 35)}{\exp(-.1(V + 35)) - 1}, \quad (26)$$

$$\beta_m(V) = 4 \exp\left(\frac{-(V + 60)}{18}\right), \quad (27)$$

$$\frac{dh}{dt} = \phi(\alpha_h(1 - h) - \beta_h h), \quad (28)$$

$$\alpha_h(V) = -.07 \exp\left(\frac{-(V + 58)}{20}\right), \quad (29)$$

$$\beta_h = \frac{1}{\exp(-0.1(V + 28)) + 1}, \quad (30)$$

$$I_K = g_K n^4 (V - E_K), \quad (31)$$

$$\frac{dn}{dt} = \phi(\alpha_n(1-n) - \beta_n n), \quad (32)$$

$$\alpha_n(V) = \frac{-0.01(V + 34)}{\exp(-.1(V + 34)) - 1}, \quad (33)$$

$$\beta_n(V) = .125 \exp\left(\frac{-(V + 44)}{80}\right), \quad (34)$$

$$I_L = g_L (V - E_L). \quad (35)$$

Table 3 shows the parameters used with these equations. I_{app} was experiment-dependent and was set so that the intrinsic firing frequency of the Wang and Buzsaki model matched the intrinsic frequency of the neuron.

Table 3. Parameters used with the Wang and Buzsaki computational model.

Parameter	Value
C_m	1.0 nF
g_{Na}	35.0 μ S
g_K	9.0 μ S
g_L	0.1 μ S
E_{Na}	55 mV
E_K	-90 mV
E_L	-65 mV
ϕ	5

REFERENCES

- Brown E, Moehlis J, and Holmes P.** On the phase reduction and response dynamics of neural oscillator populations. *Neural Computation* 16: 673-715, 2004.
- Butera R, and McCarthy M.** Analysis of real-time numerical integration methods applied to dynamic clamp experiments. *Journal of Neural Engineering* 1: 187-194, 2004.
- Butera RJ, Jr., Rinzel J, and Smith JC.** Models of respiratory rhythm generation in the pre-Botzinger complex. I. Bursting pacemaker neurons. *Journal of Neurophysiology* 82: 382-397, 1999.
- Butera RJ, Wilson CG, DelNegro CA, and Smith JC.** A methodology for achieving high-speed rates for artificial conductance injection in electrically excitable biological cells. *IEEE Transactions on Biomedical Engineering* 48: 1460-1470, 2001.
- Buzsaki G.** Hippocampal Sharp Waves - Their Origin and Significance. *Brain Research* 398: 242-252, 1986.
- Canavier CC, Baxter DA, Clark JW, and Byrne JH.** Control of multistability in ring circuits of oscillators. *Biological Cybernetics* 80: 87-102, 1999.
- Canavier CC, Butera RJ, Dror RO, Baxter DA, Clark JW, and Byrne JH.** Phase response characteristics of model neurons determine which patterns are expressed in a ring circuit model of gait generation. *Biological Cybernetics* 77: 367-380, 1997.
- Cariani PA.** Temporal codes and computations for sensory representation and scene analysis. *IEEE Transactions on Neural Networks* 15: 1100-1111, 2004.
- Chow CC.** Phase-locking in weakly heterogeneous neuronal networks. *Physica D* 118: 343-370, 1998.
- Dorval AD, Christini DJ, and White JA.** Real-time Linux dynamic clamp: A fast and flexible way to construct virtual ion channels in living cells. *Annals of Biomedical Engineering* 29: 897-907, 2001.
- Dror R, Canavier CC, Butera RJ, Clark JW, and Byrne JH.** A mathematical criterion based on phase response curves for stability in a ring of coupled oscillators. *Biological Cybernetics* 80: 11-23, 1999.
- Elson RC, Selverston AI, Abarbanel HDI, and Rabinovich MI.** Inhibitory synchronization of bursting in biological neurons: Dependence on synaptic time constant. *Journal of Neurophysiology* 88: 1166-1176, 2002.

- Engel AK, Fries P, and Singer W.** Dynamic predictions: Oscillations and synchrony in top-down processing. *Nature Reviews Neuroscience* 2: 704-716, 2001.
- Engelborghs K, Luzyanina, T., Roose, D.** Numerical bifurcation analysis of delay differential equations using DDE-BIFTOOL. *ACM Transactions on Mathematical Software* 28: 1-21, 2002.
- Ermentrout G, and Kopell N.** Oscillator death in systems of coupled neural oscillators. *SIAM Journal on Applied Mathematics* 50: 125-146, 1990a.
- Ermentrout GB.** Type I membranes, phase resetting curves, and synchrony. *Neural Computation* 8: 979-1001, 1996.
- Ermentrout GB, and Kopell N.** Multiple Pulse Interactions and Averaging in Systems of Coupled Neural Oscillators. *Journal of Mathematical Biology* 29: 195-217, 1991.
- Ermentrout GB, and Kopell N.** Oscillator death in systems of coupled neural oscillators. *SIAM Journal on Applied Mathematics* 50: 125-146, 1990b.
- Frazier W, Kandel E, Kupfermann I, Waziri R, and Coggeshall R.** Morphological and functional properties of identified neurons in the abdominal ganglion of *Aplysia californica*. *Journal of Neurophysiology* 30: 1288-1351, 1967.
- Galan RF, Ermentrout GB, and Urban NN.** Efficient estimation of phase-resetting curves in real neurons and its significance for neural-network modeling. *Physical Review Letters* 94: -, 2005.
- Glass L, and Mackey MC.** *From Clocks to Chaos : The Rhythms of Life*. Princeton, N.J.: Princeton University Press, 1988.
- Goaillard JM, and Marder E.** Dynamic clamp analyses of cardiac, endocrine, and neural function. *Physiology* 21: 197-207, 2006.
- Gramoll S, Schmidt J, and Calabrese RL.** Switching in the activity state of an interneuron that controls coordination of the hearts in the medicinal leech (*Hirudo medicinalis*). *Journal of Experimental Biology* 186: 157-171, 1994.
- Gray CM.** Synchronous oscillations in neuronal systems: Mechanisms and functions. *Journal of Computational Neuroscience* 1: 11-38, 1994.
- Gray CM.** The temporal correlation hypothesis of visual feature integration: still alive and well. *Neuron* 24: 31-47, 1999.
- Gross J, Timmermann L, Kujala J, Dirks M, Schmitz F, Salmelin R, and Schnitzler A.** The neural basis of intermittent motor control in humans. *PNAS* 99: 2299-2302, 2002.

- Hansel D, Mato G, and Meunier C.** Phase Dynamics for Weakly Coupled Hodgkin-Huxley Neurons. *Europhysics Letters* 23: 367-372, 1993.
- Hansel D, Mato G, and Meunier C.** Synchrony in excitatory neural networks. *Neural Computation* 7: 307-337, 1995.
- Hutchinson WD, Dostrovsky J, Walters J, Courtemanche R, Borraud T, Goldberg J, and Brown P.** Neuronal oscillations in the basal ganglia and movement disorders: Evidence from whole animal and human recordings. *Journal of Neuroscience* 24: 9240-9243, 2004.
- Jalife J.** Mutual Entrainment and Electrical Coupling as Mechanisms for Synchronous Firing of Rabbit Sino-Atrial Pace-Maker Cells. *Journal of Physiology-London* 356: 221-243, 1984.
- Kandel ER.** *Cellular Basis of Behavior*. San Francisco: W. H. Freeman and Company, 1976.
- Kinard TA, de Vries G, Sherman A, and Satin LS.** Modulation of the bursting properties of single mouse pancreatic beta-cells by artificial conductances. *Biophysical Journal* 76: 1423-1435, 1999.
- Kiss IZ, Zhai Y, and Hudson JL.** Emerging coherence in a population of chemical oscillators. *Science* 296: 1676-1678, 2002.
- Kozyreff G, Vladimirov AG, and Mandel P.** Global coupling with time delay in an array of semiconductor lasers. *Physical Review Letters* 85: 3809-3812, 2000.
- Kumar R, Wilders R, Joyner RW, Jongsma HJ, Verheijck EE, Golod DA, van Ginneken AC, and Goolsby WN.** Experimental model for an ectopic focus coupled to ventricular cells. *Circulation* 94: 833-841, 1996.
- Kuramoto Y.** *Chemical oscillations, waves, and turbulence*. New York: Springer-Verlag, 1984.
- Le Masson G.** From conductances to neural network properties: Analysis of simple circuits using the hybrid network method. *Progress in Biophysics and Molecular Biology* 64: 201-220, 1995.
- Lien C, and Jonas P.** Kv3 potassium conductance is necessary and kinetically optimized for high-frequency action potential generation in hippocampal interneurons. *Journal of Neuroscience* 23: 2058-2068, 2003.
- Llinas R, and Ribary U.** Coherent 40-Hz Oscillation Characterizes Dream State in Humans. *PNAS* 90: 2078-2081, 1993.

- Luo C, Clark JW, Jr., Canavier CC, Baxter DA, and Byrne JH.** Multimodal behavior in a four neuron ring circuit: mode switching. *IEEE Transactions on Biomedical Engineering* 51: 205-218, 2004.
- Ma M, and Koester J.** The role of K⁺ currents in frequency-dependent spike broadening in Aplysia R20 neurons: a dynamic-clamp analysis. *Journal of Neuroscience* 16: 4089-4101, 1996.
- Manor Y, and Nadim F.** Frequency regulation demonstrated by coupling a model and a biological neuron. *Neurocomputing* 38: 269-278, 2001.
- Maran SK, and Canavier CC.** Personal Communication. 2007.
- Merriam EB, Netoff TI, and Banks MI.** Bistable network behavior of layer I interneurons in auditory cortex. *Journal of Neuroscience* 25: 6175-6186, 2005.
- Mirollo RE, and Strogatz SH.** Synchronization of Pulse-Coupled Biological Oscillators. *SIAM Journal on Applied Mathematics* 50: 1645-1662, 1990.
- Netoff TI, Acker CD, Bettencourt JC, and White JA.** Beyond two-cell networks: experimental measurement of neuronal responses to multiple synaptic inputs. *Journal of Computational Neuroscience* 18: 287-295, 2005a.
- Netoff TI, Banks MI, Dorval AD, Acker CD, Haas JS, Kopell N, and White JA.** Synchronization in hybrid neuronal networks of the hippocampal formation. *Journal of Neurophysiology* 93: 1197-1208, 2005b.
- Nowotny T, Zhigulin VP, Selverston AI, Abarbanel HDI, and Rabinovich MI.** Enhancement of synchronization in a hybrid neural circuit by spike-timing dependent plasticity. *Journal of Neuroscience* 23: 9776-9785, 2003.
- Oprisan SA, Prinz AA, and Canavier CC.** Phase resetting and phase locking in hybrid circuits of one model and one biological neuron. *Biophysical Journal* 87: 2283-2298, 2004.
- Palva JM, Palva S, and Kaila K.** Phase synchrony among neuronal oscillations in the human cortex. *Journal of Neuroscience* 25: 3962-3972, 2005.
- Pantaleone J.** Stability of incoherence in an isotropic gas of oscillating neutrinos. *Physical Review D* 58: 073002, 1998.
- Park MR, Kita H, Klee MR, and Oomura Y.** Bridge Balance in Intracellular-Recording - Introduction of the Phase-Sensitive Method. *Journal of Neuroscience Methods* 8: 105-125, 1983.
- Pavlidis T.** *Biological Oscillators: Their Mathematical Analysis*. New York: Academic Press, 1973.

- Perkel DH, Schulman JH, Bullock TH, Moore GP, and Segundo JP.** Pacemaker Neurons: Effects Of Regularly Spaced Synaptic Input. *Science* 145: 61-63, 1964.
- Pervouchine DD, Netoff TI, Rotstein HG, White JA, Cunningham MO, Whittington MA, and Kopell NJ.** Low-dimensional maps encoding dynamics in entorhinal cortex and hippocampus. *Neural Computation* 18: 2617-2650, 2006.
- Pfeuty B, Mato G, Golomb D, and Hansel D.** The combined effects of inhibitory and electrical synapses in synchrony. *Neural Computation* 17: 633-670, 2005.
- Pinto RD, Elson RC, Szucs A, Rabinovich MI, Selverston AI, and Abarbanel HDI.** Extended dynamic clamp: controlling up to four neurons using a single desktop computer and interface. *Journal of Neuroscience Methods* 108: 39-48, 2001.
- Poliakov AV, Powers RK, and Binder MD.** Functional identification of the input-output transforms of motoneurons in the rat and cat. *Journal of Physiology* 504 (Pt 2): 401-424, 1997.
- Preyer A.** A hardware implementation of the dynamic clamp. In: *School of Electrical and Computer Engineering*. Atlanta: Georgia Institute of Technology, 2002.
- Preyer AJ, and Butera RJ.** Neuronal oscillators in aplysia californica that demonstrate weak coupling in vitro. *Physical Review Letters* 95: 138103, 2005.
- Prinz AA, Abbott LF, and Marder E.** The dynamic clamp comes of age. *Trends in Neurosciences* 27: 218-224, 2004.
- Raikov I, Preyer A, and Butera RJ.** MRCI: a flexible real-time dynamic clamp system for electrophysiology experiments. *Journal of Neuroscience Methods* 132: 109-123, 2004.
- Robinson HP, and Kawai N.** Injection of digitally synthesized synaptic conductance transients to measure the integrative properties of neurons. *Journal of Neuroscience Methods* 49: 157-165, 1993.
- Schnitzler A, and Gross J.** Normal and pathological oscillatory communication in the brain. *Nature Reviews Neuroscience* 6: 285-296, 2005.
- Sharp AA, O'Neil MB, Abbott LF, and Marder E.** Dynamic Clamp - Computer-Generated Conductances in Real Neurons. *Journal of Neurophysiology* 69: 992-995, 1993a.
- Sharp AA, O'Neil MB, Abbott LF, and Marder E.** The dynamic clamp: Artificial conductances in biological neurons. *Trends in Neurosciences* 16: 389-394, 1993b.
- Sharp AA, Skinner FK, and Marder E.** Mechanisms of oscillation in dynamic clamp constructed two-cell half-center circuits. *Journal of Neurophysiology* 76: 867-883, 1996.

- Sherman-Gold R** editor. *The Axon CNS Guide to Electrophysiology and Biophysics*. Union City, CA: Molecular Devices Corporation, 1993.
- Sherman A, and Rinzel J**. Rhythmogenic effects of weak electrotonic coupling in neuronal models. *PNAS* 89: 2471-2474, 1992.
- Sherman A, Rinzel J, and Keizer J**. Emergence of organized bursting in clusters of pancreatic beta-cells by channel sharing. *Biophysical Journal* 54: 411-425, 1988.
- Singer W**. Neuronal synchrony: a versatile code for the definition of relations? *Neuron* 24: 49-65, 111-125, 1999.
- Skinner FK, Chung JY, Ncube I, Murray PA, and Campbell SA**. Using heterogeneity to predict inhibitory network model characteristics. *Journal of Neurophysiology* 93: 1898-1907, 2005.
- Skinner FK, Kopell N, and Marder E**. Mechanisms for oscillation and frequency control in reciprocally inhibitory model neural networks. *Journal of Computational Neuroscience* 1: 69-87, 1994.
- Stelt Ovd, Belger A, and Lieberman JA**. Macroscopic fast neuronal oscillations and synchrony in schizophrenia. *PNAS* 101: 2004.
- Steriade M**. Synchronized activities of coupled oscillators in the cerebral cortex and thalamus at different levels of vigilance. *Cerebral Cortex* 7: 583-604, 1997.
- Strogatz SH**. From Kuramoto to Crawford: exploring the onset of synchronization in populations of coupled oscillators. *Physica D* 143: 1-20, 2000.
- Terman D, Kopell N, and Bose A**. Dynamics of two mutually coupled slow inhibitory neurons. *Physica D-Nonlinear Phenomena* 117: 241-275, 1998.
- Timofeev I, and Steriade M**. Neocortical seizures: Initiation, development and cessation. *Neuroscience* 123: 299-336, 2004.
- Ulrich D, and Huguenard JR**. Gamma-aminobutyric acid type B receptor-dependent burst-firing in thalamic neurons: a dynamic clamp study. *PNAS* 93: 13245-13249, 1996.
- Van Vreeswijk C, Abbott LF, and Ermentrout GB**. When inhibition not excitation synchronizes neural firing. *Journal of Computational Neuroscience* 1: 313-321, 1994.
- Verheijck EE, Wilders R, Joyner RW, Golod DA, Kumar R, Jongsma HJ, Bouman LN, and van Ginneken AC**. Pacemaker synchronization of electrically coupled rabbit sinoatrial node cells. *Journal of General Physiology* 111: 95-112, 1998.

- Wang XJ, and Buzsaki G.** Gamma oscillation by synaptic inhibition in a hippocampal interneuronal network model. *Journal of Neuroscience* 16: 6402-6413, 1996.
- Wang XJ, and Rinzel J.** Alternating and Synchronous Rhythms in Reciprocally Inhibitory Model Neurons. *Neural Computation* 4: 84-97, 1992.
- Ward LM.** Synchronous neural oscillations and cognitive processes. *Trends in Cognitive Science* 7: 1926-1929, 2003.
- White JA, Chow CC, Ritt J, Soto-Trevino C, and Kopell N.** Synchronization and oscillatory dynamics in heterogeneous, mutually inhibited neurons. *Journal of Computational Neuroscience* 5: 5-16, 1998.
- Wiesenfeld K, Colet P, and Strogatz SH.** Synchronization transitions in a disordered Josephson series array. *Physical Review Letters* 76: 404-407, 1996.
- Wilders R.** Dynamic clamp: a powerful tool in cardiac electrophysiology. *Journal of Physiology-London* 576: 349-359, 2006.
- Wilson CJ, and Park MR.** Capacitance compensation and bridge balance adjustment in intracellular recording from dendritic neurons. *Journal of Neuroscience Methods* 27: 51-75, 1989.
- Winfree AT.** Biological rhythms and the behavior of populations of coupled oscillators. *Journal of Theoretical Biology* 16: 15-42, 1967.
- Winfree AT.** *The Geometry of Biological Time*. New York: Springer-Verlag, 2001.
- Zhang Y, Oliva R, Gisselmann G, Hatt H, Guckenheimer J, and Harris-Warrick RM.** Overexpression of a hyperpolarization-activated cation current (I_h) channel gene modifies the firing activity of identified motor neurons in a small neural network. *Journal of Neuroscience* 23: 9059-9067, 2003.

VITA

Amanda Jervis Preyer was born in Concord, Massachusetts, and grew up in Rockville, Maryland. After graduating from Thomas S. Wootton high school in Maryland, she obtained a B.S. in Electrical Engineering at Lafayette College in Easton, Pennsylvania, graduating in May of 1999. She then worked for a year doing printed circuit board design at DSP Tools, Inc. before starting graduate school at Georgia Tech in August 2000. She received her M.S. in Electrical and Computer Engineering in August 2002, and became a Research Engineer in the same lab. In 2003, she returned to student status and completed her Ph.D. in Electrical and Computer Engineering in August 2007.